

# Numerical simulations of swirling electrovortex flows in cylinders

S. Bénard<sup>1,†</sup>, W. Herreman<sup>1</sup>, J.L. Guermond<sup>2</sup> and C. Nore<sup>1</sup>

<sup>1</sup>Université Paris-Saclay, CNRS, LISN, 91400 Orsay, France

<sup>2</sup>Department of Mathematics, Texas A&M University 3368 TAMU, College Station, TX 77843-3368, USA

(Received 30 November 2021; revised 5 July 2022; accepted 29 August 2022)

We study swirling electrovortex flows in a cylinder filled with GaInSn metal using axisymmetric and large-scale three-dimensional numerical simulations. In our set-up electrical currents enter and exit the cell symmetrically through wires and the result is a von Kármán-like flow. Three inductionless and an inductive flow regimes are identified. Scaling laws for the magnitude of the velocity in each of these regimes are obtained both numerically and explained theoretically. We study how the aspect ratio of the cell affects the flow and how symmetrically wired cells are different from asymmetrical wired cells. We vary the radius of the connecting wires and propose a simple model that captures how the flow's intensity varies with the wire radius.

**Key words:** magnetic fluids, transition to turbulence, turbulent mixing

## 1. Introduction

When an intense electrical current is injected into a liquid metal domain by using a thin wire, fluid motion is generated by the Lorentz force in the liquid metal. These flows are called electrovortex flows (EVFs) and the reader is referred to Bojarevičs *et al.* (1989) for an extensive review and early references on this topic.

Recently, different types of EVFs have been investigated within the applied context of liquid metal batteries (LMBs); see Kelley & Weier (2018) for a review. The idea is that EVFs can enhance the mixing of the alloy layer and, hence, contribute to improving the battery efficiency. This idea was first proposed in Kelley & Sadoway (2014) and triggered the numerical studies of Ashour *et al.* (2018), Weber *et al.* (2018), Herreman *et al.* (2020). Small vertical magnetic fields can significantly modify the EVF, giving it a swirling character (see, for example, Millere, Sharamkin & Shcherbinin 1980; Bojarevics, Millere & Chaikovskiy 1981; Davidson *et al.* 1999; Davidson 2001). In LMBs it was shown by

† Email address for correspondence: [sabrina.benard@universite-paris-saclay.fr](mailto:sabrina.benard@universite-paris-saclay.fr)

Weber *et al.* (2020), Herreman *et al.* (2021) that such swirling EVFs are intense enough to enhance mixing.

In addition to being dedicated to the analysis of alloy mixing in LMBs, Herreman *et al.* (2021) also reports results obtained by performing highly resolved three-dimensional (3-D) numerical simulations of turbulent swirling EVFs using the code SFEMaNS (Guermond *et al.* 2007, 2009; Cappanera *et al.* 2018). These simulations have been done at high Reynolds numbers (up to  $10^4$ ) without using any turbulence model. Other numerical studies on EVFs often use turbulence models ( $k-\epsilon$  in Davidson *et al.* (1999) for example) and early work is often restricted to axisymmetric simulations. One interesting result established in Herreman *et al.* (2021) is that the intensity of the swirling EVF in a cylindrical cell can obey the following scaling law:

$$U \sim \left(\frac{JB}{\rho}\right)^{2/3} \frac{R}{\nu^{1/3}}. \quad (1.1)$$

Here  $J$  is the typical current density in the bulk of the liquid metal,  $B$  is the imposed axial magnetic field,  $\rho$  and  $\nu$  are the metal's density and kinematic viscosity, respectively, and  $R$  is the radius of the cylindrical cell. This result is obtained in Herreman *et al.* (2021) by invoking a three-term balance between the inertia, the viscous and the Lorentz forces in a thin boundary layer near the electrical contact. A slightly different scaling law for the intensity of the swirling EVF was suggested in Davidson *et al.* (1999), i.e.

$$U \sim \left(\frac{JBR}{\rho}\right)^{5/9} \left(\frac{R}{\nu}\right)^{1/9} \quad \text{or} \quad U \sim \left(\frac{JBR}{\rho}\right)^{1/2}. \quad (1.2)$$

The above scaling laws are not explicitly written in this way in Davidson *et al.* (1999), but can be easily recovered (see Appendix A). Since the 5/9 law is clearly observed in the axisymmetric  $k-\epsilon$  model simulations reported in Davidson *et al.* (1999), one is led to wonder why a different scaling law is observed in Herreman *et al.* (2021). Recent work by Kolesnichenko *et al.* (2020) also studies swirling EVFs in 3-D simulations and with a  $k-\omega$  turbulence model and finds a scaling law that is somewhere in between the 2/3 and 5/9 laws.

The above observations have led us to do a systematic and fundamental study on swirling EVFs, outside the context of LMBs. What are the different scaling regimes that can be observed in swirling EVFs and how does this depend on  $JB/\rho$  and  $\nu$ ? What happens when the imposed axial magnetic field is large, when inductive effects are no longer negligible? How are the scaling laws influenced by the axisymmetry assumption? To answer these questions, we have performed numerical simulations of the unsteady swirling EVF at high Reynolds numbers using our numerical solver SFEMaNS.

At variance with Millere *et al.* (1980), Liu *et al.* (2020), Kolesnichenko *et al.* (2020), Herreman *et al.* (2020), Herreman *et al.* (2021), where there is only one 'thin' wire bringing the current to the cell (i.e. the current is extracted from the whole upper disk closing the cell or from the whole side), the majority of the simulations reported in the present article are done by bringing and extracting the current through two cylindrical wires whose axes are aligned with that of the cell; one is connected to the bottom of the cell and the other one is connected to the top; see figure 1. This setting has also been studied in Weber *et al.* (2015). In the presence of an axial magnetic field  $Be_z$ , the azimuthal force densities  $-j_r Be_\theta$  in the top and bottom halves of the cell have opposite directions and they are also of equal strength. This  $R_\pi$ -symmetric forcing produces a counter-rotating EVF that should have many structural similarities with von Kármán flows, which were the subject

## Simulations of swirling electrovortex flows in cylinders

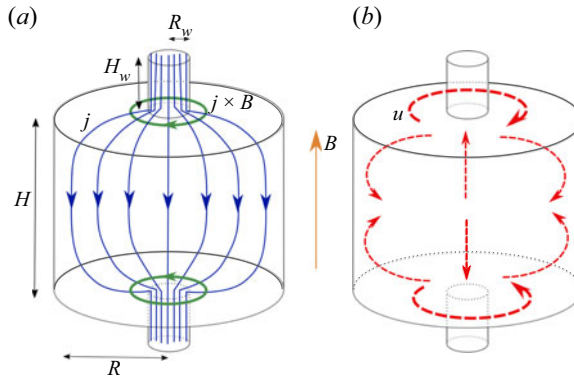


Figure 1. Sketch of the investigated set-up and flow. (a) A pair of solid copper wires injects and extracts an electrical current in a cylinder filled with liquid GaInSn eutectic metal. The current density lines spread out as shown by the blue lines. The set-up is immersed in a vertical magnetic field  $B$ . The Lorentz force  $\mathbf{j} \times B\mathbf{e}_z$  is predominantly azimuthal, localized near the rim of the electrical contact and  $R_\pi$  symmetric. (b) The EVF that is thus produced is structurally similar to a von Kármán flow. The fluid rotates in opposite directions in the top and bottom halves of the cell and is pumped towards the wires along the axis.

of many hydrodynamical and magnetohydrodynamical investigations (see, e.g. Nore *et al.* 2003, 2004; Monchaux *et al.* 2007; Berhanu *et al.* 2007). We are then led to consider the following two additional questions. Does the considered set-up indeed produce a von Kármán-like flow? Does the symmetry of the forcing affect the scaling laws of the swirling EVF?

The objective of the paper is to answer the above questions using numerical simulations. We start by defining the model in § 2. In § 3 we study the influence of the control parameters  $J$ ,  $B$ ,  $\nu$  on the intensity of the EVF in a cell with fixed geometry. We show that the flow is indeed von Kármán-like and describe and explain the various scaling regimes. In § 4 we study geometrical influences on EVFs. We vary the radius of the wires and propose a simple model to describe the variation intensity of the swirling EVF with this radius. We also vary the height of the cell and study the impact of asymmetrical current injection/extraction. We conclude the paper and summarize our findings in § 5.

### 2. Model and discretization

The configuration investigated in the paper is described in figure 1. A cylinder of radius  $R$  and height  $H$  is filled with liquid GaInSn eutectic alloy. Two identical cylindrical copper wires of radius  $R_w$  and height  $H_w$  are electrically connected to the fluid, one is attached at the top of the cell and the other one is attached at the bottom of the cell. The axes of the two wires are aligned with the vertical axis of the cell. An external vertical magnetic field  $B\mathbf{e}_z$  is applied and an electrical current of intensity  $I$  is driven through the cell. Let  $J = I/\pi R^2$  be the reference current density; this would be the current density if the current were homogenous inside the cylinder. We systematically use the cylindrical coordinates  $(r, \theta, z)$  with the convention that the equatorial plane of the cell is defined by  $z = 0$ .

We model the evolution of the velocity and the electromagnetic fields in the liquid GaInSn alloy by the incompressible magneto-hydrodynamics equations,

$$\rho(\partial_t \mathbf{u} + (\mathbf{u} \cdot \nabla) \mathbf{u}) = -\nabla p + \rho \nu \Delta \mathbf{u} + \mathbf{j} \times \mathbf{b}, \quad (2.1a)$$

$$\partial_t \mathbf{b} = \nabla \times (\mathbf{u} \times \mathbf{b}) + (\mu_0 \sigma)^{-1} \Delta \mathbf{b}, \quad (2.1b)$$

$$\nabla \cdot \mathbf{u} = 0, \tag{2.1c}$$

$$\nabla \cdot \mathbf{b} = 0. \tag{2.1d}$$

Here  $\mathbf{u}$  is the velocity of the fluid,  $p$  is the pressure,  $\mathbf{j} = \mu_0^{-1} \nabla \times \mathbf{b}$  is the current density and  $\mathbf{b}$  is the magnetic field. The symbol  $\mu_0$  denotes the magnetic permeability of vacuum. The density  $\rho$ , the kinematic viscosity  $\nu$  and the electrical conductivity  $\sigma$  of the GaInSn eutectic alloy at  $T = 303$  K are taken from Plevachuk *et al.* (2014),

$$\rho = 6345 \text{ kg m}^{-3}, \quad \nu = 3.2 \times 10^{-7} \text{ m}^2 \text{ s}^{-1}, \quad \sigma = 3.24 \times 10^6 \text{ S m}^{-1}. \tag{2.2a-c}$$

The magnetic field in the solid copper wires,  $\mathbf{b}_w$ , satisfies the induction equation

$$\partial_t \mathbf{b}_w = (\mu_0 \sigma_w)^{-1} \Delta \mathbf{b}_w, \tag{2.3a}$$

$$\nabla \cdot \mathbf{b}_w = 0, \tag{2.3b}$$

where  $\sigma_w = 5.96 \times 10^7 \text{ S m}^{-1}$  is the electrical conductivity of the copper wires.

The fluid is supposed to be initially at rest. We impose the no-slip boundary condition on the velocity on the entire surface of the cylinder. We also use the following boundary conditions and transmission conditions for the magnetic field:

$$\left. \begin{aligned} b_z|_{r=R} &= B, & b_\theta|_{r=R} &= \mu_0 J R / 2, \\ b_r|_{z=\pm H/2} &= 0, & b_\theta|_{z=\pm H/2} &= \mu_0 J R^2 / 2r, & \forall r \in [R_w, R], \\ \mathbf{e}_z \times (\mathbf{b} - \mathbf{b}_w)|_{z=\pm H/2} &= 0, & \mathbf{e}_z \times ((\mathbf{j}/\sigma) - (\mathbf{j}_w/\sigma_w))|_{z=\pm H/2} &= 0, & \forall r \in [0, R_w], \\ b_{w,z}|_{r=R_w} &= B, & b_{w,\theta}|_{r=R_w} &= \mu_0 J R^2 / 2R_w, \\ b_{w,r}|_{z=\pm(H/2+H_w)} &= 0, & b_{w,\theta}|_{z=\pm(H/2+H_w)} &= \mu_0 J R^2 r / 2R_w^2. \end{aligned} \right\} \tag{2.4}$$

Here  $\mathbf{j}_w = \mu_0^{-1} \nabla \times \mathbf{b}_w$  is the current density in the wire. The above conditions are known to yield a suitable approximation of the EVF in devices surrounded by vacuum as long as the magnetic Reynolds number remains small (Herreman *et al.* 2019, 2021). These simplified conditions avoid having to calculate the external potential magnetic field outside the cylinder.

The solution to the problem defined in the previous section is approximated by using the massively parallel code SFEMaNS. This code has been thoroughly validated. The reader is referred to Guermond *et al.* (2007), Guermond *et al.* (2009), Cappanera *et al.* (2018) for the algorithmic details and the verification and validation tests. The code SFEMaNS uses a Fourier decomposition in the azimuthal direction and a finite element representation in the meridional plane. Every field  $A$ , scalar- or vector-valued, is decomposed as

$$A(r, z, \theta, t) = \sum_{m=0}^{M-1} A_m^c(r, z, t) \cos(m\theta) + \sum_{m=1}^{M-1} A_m^s(r, z, t) \sin(m\theta). \tag{2.5}$$

Here  $A_m^c(r, z, t)$  and  $A_m^s(r, z, t)$  are finite element functions, and  $M$  is the number of complex Fourier modes. The outputs delivered by the code are either temporal snapshots or global quantities. Denoting by  $\langle \cdot \cdot \rangle_V$  the volume average over the entire cylindrical fluid domain, we are going to use the following global quantities:

$$\mathbf{u} = \sqrt{\langle \|\mathbf{u}\|^2 \rangle_V}, \quad u_{max} = \max_{x \in V} \|\mathbf{u}(\mathbf{x}, t)\|. \tag{2.6a,b}$$

Here  $\|\mathbf{u}\|^2 = \int_V (u_r^2(\mathbf{x}, t) + u_\theta^2(\mathbf{x}, t) + u_z^2(\mathbf{x}, t)) \text{ d}V$ , with  $V$  the volume of the entire cylindrical fluid domain.

Letting  $\delta_{kl}$  be the Kronecker symbol, we further define the following quantities for all  $m \in \{0, \dots, M - 1\}$  to measure the modal content of the flow:

$$u_m = \sqrt{0.5 \langle (1 + \delta_{m,0}) \| \mathbf{u}_m^c \|^2 + (1 - \delta_{m,0}) \| \mathbf{u}_m^s \|^2 \rangle_V}. \quad (2.7)$$

We measure the toroidal and poloidal parts of the axisymmetric component of the flow by using the following indicators:

$$u_{tor} = \sqrt{\langle (u_{0,\theta}^c)^2 \rangle_V}, \quad u_{pol} = \sqrt{\langle (u_{0,r}^c)^2 + (u_{0,z}^c)^2 \rangle_V}. \quad (2.8a,b)$$

We finally use bars over the above indicators to mean that the indicators have been averaged over time; for instance,  $\bar{u}$  and  $\bar{u}_{max}$  are the time averages of  $u$  and  $u_{max}$ . The time-averaging operation allows us to define the following non-dimensional quantities:

$$\bar{Re} = \frac{\bar{u}R}{\nu}, \quad \bar{\Pi} = \frac{\sigma \bar{u}B}{J}. \quad (2.9a,b)$$

The parameter  $\bar{Re}$  is a Reynolds number, and  $\bar{\Pi}$  measures the ratio of the inductive currents over the imposed current. The inverse of  $\bar{\Pi}$  is also named the load factor (Sutton & Sherman 1965; Geindreau & Auriault 2002).

### 3. Influence of $J$ , $B$ and $\nu$ on swirling EVFs

In this section we report the results of a series of simulations in the set-up with the following fixed geometry  $(R, H, R_w, H_w) = (10, 18, 2, 4)$  cm. The aspect ratio  $H/R = 1.8$  is chosen to be identical to that used in the von Kármán sodium experiment (Monchaux *et al.* 2007; Berhanu *et al.* 2007). We vary  $J$ ,  $B$  and  $\nu$  and compare axisymmetric and 3-D simulations.

#### 3.1. Variable $J$ , axisymmetric study

We first set the value of imposed magnetic field to be  $B = 1$  mT and we use the following value for the kinematic viscosity  $\nu = 3.2 \times 10^{-7} \text{ m}^2 \text{ s}^{-1}$ . We vary the imposed electrical current  $J$  as detailed in the leftmost column in table 1. We also provide in this table the main numerical parameters used for each numerical simulation: the time step  $\Delta t$ , the meridional mesh size  $\Delta l$  and the measured values of  $\bar{Re}$  and  $\bar{\Pi}$ . The meshes used are non-uniform, the two values of  $\Delta l$  indicate the smallest and largest mesh sizes. All the simulations reported in this section are done by taking  $M = 1$  in the azimuthal Fourier approximation; i.e. the flow is forced to be axisymmetric.

We show in figure 2(a) the time evolution of the volume-averaged velocity,  $u$ , in log scale for the ordinate axis, for different values of  $J$ . We observe that the flow reaches a steady state for  $J = 5, 10 \text{ A m}^{-2}$ . For  $J = 50, 100 \text{ A m}^{-2}$ , the flow seems to converge to a state that is almost steady (the oscillations around this state are small), but a transition occurs at later times, and the second state that is then reached is characterized by large fluctuations (e.g. at  $t \approx 7200 \text{ s}$  for  $J = 50 \text{ A m}^{-2}$ ). For the largest values of the current,  $J = 500, 2000 \text{ A m}^{-2}$ , the flow starts oscillating after a very short transient. The time- and space-averaged velocity,  $\bar{u}$ , increases monotonously with  $J$ , as can be seen in figure 2(b). For low  $J$ , we clearly observe a power law  $\bar{u} \sim J^1$ . For intermediate  $J$ , the scaling  $\bar{u} \sim J^{2/3}$  is perhaps visible over a short interval. At high  $J$ , we can observe a power law  $\bar{u} \sim J^{1/2}$  or  $J^{5/9}$ . In figure 2(c) we show the ratio  $\bar{u}_{pol}/\bar{u}_{tor}$  as a function of  $J$ . This ratio is small

$J(\text{A m}^{-2})$	$\Delta l$ (m)	$\Delta t$ (s) <sup>(a)</sup>	$\overline{Re}^{(a)}$	$\overline{\Pi}^{(a)}$	$\Delta t$ (s) <sup>(b)</sup>	$\overline{Re}^{(b)}$	$\overline{\Pi}^{(b)}$
$M = 20$							
$10^{-2}$	0.0025 $\rightarrow$ 0.005	2	0.25	0.27			
$10^{-1}$	0.0025 $\rightarrow$ 0.005	$5 \times 10^{-1}$	2.5	0.27			
1	0.0025 $\rightarrow$ 0.005	$1 \times 10^{-1}$	22	0.23	$1 \times 10^{-1}$	22	0.23
5	0.0025 $\rightarrow$ 0.005	$5 \times 10^{-2}$	85	0.18	$5 \times 10^{-2}$	77	0.16
10	0.0025 $\rightarrow$ 0.005	$2 \times 10^{-2}$	144	0.15	$5 \times 10^{-2}$	124	0.13
25	0.0025 $\rightarrow$ 0.005				$5 \times 10^{-2}$	216	0.09
50	0.0025 $\rightarrow$ 0.005	$4 \times 10^{-2}$	409	0.086	$3 \times 10^{-2}$	328	0.068
100	0.0005 $\rightarrow$ 0.0025	$1 \times 10^{-2}$	603	0.063	$1 \times 10^{-2}$	499	0.052
500	0.0005 $\rightarrow$ 0.0025	$4 \times 10^{-3}$	1502	0.031	$6 \times 10^{-3}$	1180	0.024
2000	0.0005 $\rightarrow$ 0.0025	$1 \times 10^{-3}$	2964	0.016	$2 \times 10^{-3}$	2519	0.013
$M = 40$							
100	0.0005 $\rightarrow$ 0.0025	$1 \times 10^{-2}$	603	0.063	$1 \times 10^{-2}$	499	0.052
500	0.0005 $\rightarrow$ 0.0025	$4 \times 10^{-3}$	1502	0.031	$6 \times 10^{-3}$	1180	0.024
2000	0.0005 $\rightarrow$ 0.0025	$1 \times 10^{-3}$	2964	0.016	$2 \times 10^{-3}$	2519	0.013

Table 1. Numerical parameters for the simulations with variable  $J$ . Mesh size  $\Delta l$  (non-uniform meshes, smallest  $\rightarrow$  largest mesh size), time step  $\Delta t$ , non-dimensional numbers  $\overline{Re} = \bar{u}R/\nu$  and  $\overline{\Pi} = \sigma \bar{u}B/J$ . (a) Axisymmetric simulations, (b) 3-D simulations with  $M = 20$  or  $M = 40$ .

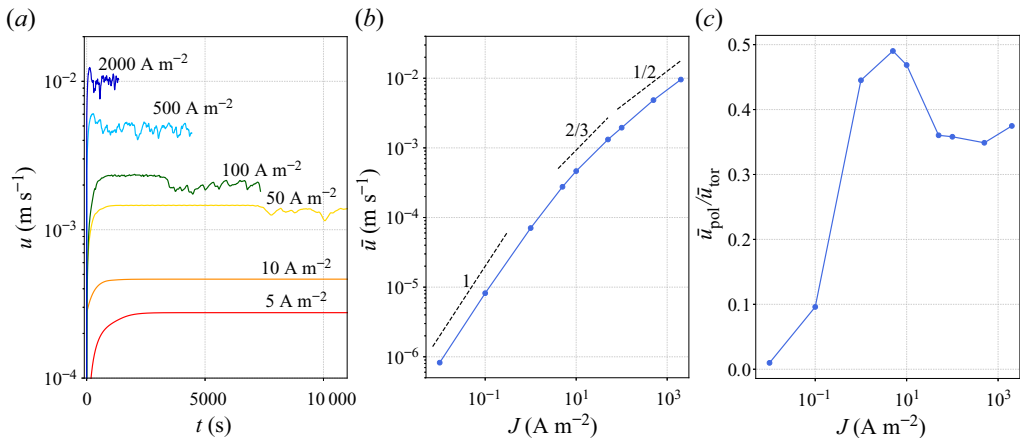


Figure 2. Variable  $J$ , axisymmetric simulations. (a) Time evolution of the volume-averaged velocity  $u$  for different values of  $J$ . (b) Time- and space-averaged velocity  $\bar{u}$  as a function of  $J$  (time average done after the transient). (c) Ratio  $\bar{u}_{\text{pol}}/\bar{u}_{\text{tor}}$  as a function of  $J$ .

for  $J = 0.01 \text{ A m}^{-2}$ . It then increases as  $J$  grows until reaching a maximum almost equal to 0.5 at  $J = 5 \text{ A m}^{-2}$ . For higher values of  $J$ , it first decreases and eventually fluctuates around a plateau. We also observe that the magnitude of the toroidal component of the velocity always dominates that of the poloidal component.

In figure 3 we show the spatial structure of the axisymmetric EVF at various values of the current. We show in figures 3(a) and 3(b) 3-D streamlines of the velocity field coloured by the magnitude of the velocity. The geometric organisation of the flow is similar to that of the von Kármán flows found in (Nore *et al.* 2003): the fluid is pumped along the axis from the equatorial plane towards the top and bottom caps; it is then expelled outwards

along the two cylindrical caps and returns back to the equatorial plane along the side wall of the cell in a spiral fashion; the spiral motion of the fluid in the upper half of the cell is opposite to that of the fluid in the lower half. For  $J = 5 \text{ A m}^{-2}$ , the velocity field is stationary and  $R_\pi$  symmetric, meaning that

$$\begin{pmatrix} u_r \\ u_\theta \\ u_z \end{pmatrix} (r, \theta, z) = \begin{pmatrix} u_r \\ -u_\theta \\ -u_z \end{pmatrix} (r, -\theta, -z). \quad (3.1)$$

For  $J = 500 \text{ A m}^{-2}$ , the invariance under the  $R_\pi$  symmetry is broken and the streamlines of the velocity form a chaotic web. We show in [figure 3\(c\)](#) the magnitude of the velocity  $\|\mathbf{u}\|$  in meridional planes for various values of the current  $J$ . For the smallest value of the current,  $J = 0.1 \text{ A m}^{-2}$ , the flow is steady and is the most intense near the rim of the electrical contact with the wires. Up until  $J = 10 \text{ A m}^{-2}$ , the intensity of the flow gradually increases close to the vertical axis while still being invariant under the  $R_\pi$  symmetry. At  $J = 50 \text{ A m}^{-2}$  and above this value the system becomes time dependent: the  $R_\pi$  symmetry is broken. The flow eventually becomes chaotic for large values of  $J$ . The intensity of the flow is notably small near the axis and in two regions close to the two contacts with the connecting wires.

The large change in the spatial structure of the flow between  $J = 10 \text{ A m}^{-2}$  and  $J = 50 \text{ A m}^{-2}$  indicates that a symmetry-breaking bifurcation occurs for a critical value  $J_c$  in the interval  $[10, 50] \text{ A m}^{-2}$ . [Figure 4\(a\)](#) shows two snapshots of the magnitude of the velocity,  $\|\mathbf{u}\|$ , for  $J = 50 \text{ A m}^{-2}$ . The flow is (quasi)-symmetric, (quasi)-steady and intense close to the axis at  $t = 4000 \text{ s}$ , but steadiness is lost and the symmetry is broken at  $t = 30\,000 \text{ s}$ . Note also that at this time the magnitude of the velocity is small in a small cylinder close to the axis. To measure the critical current density  $J_c^{axi}$  of the bifurcation, we calculate the volume average of the kinetic energy in the top half and in the bottom half of the cell. The volume average computed over the upper half is denoted  $E_{top}$  and the volume average computed over the lower half is denoted  $E_{bot}$ . If, starting from 0, the difference  $|E_{top} - E_{bot}|$  grows in time, we conclude that there is a loss of symmetry. We use this quantity to measure the growth rate of the instability. This concept is illustrated in the inset of [figure 4\(b\)](#) where we show how  $|E_{top} - E_{bot}|$  increases exponentially with time before reaching a plateau. Using a semi-logarithmic scale, we measure the growth rate  $\lambda$  as the slope of the straight line fitting the logarithm of  $|E_{top} - E_{bot}|$  in the transient regime. The growth rates computed with seven values of  $J$  are shown in [figure 4\(b\)](#). Using linear extrapolation, we estimate that the instability threshold is  $J_c^{axi} \approx 17 \text{ A m}^{-2}$ .

### 3.2. Variable $J$ , 3-D study

We now present the results of 3-D simulations done with  $M = 20$  or  $M = 40$  Fourier modes. We focus on  $M = 20$  and then justify why we use 20 modes by comparing cases with 20 and 40 modes.

In [figure 5](#) we show the time evolution of the volume-averaged velocity  $u$  and its Fourier components  $u_0, u_1, u_2, u_3$ . For  $J = 1 \text{ A m}^{-2}$ , the system remains axisymmetric. At  $J = 5 \text{ A m}^{-2}$  a first symmetry-breaking bifurcation has occurred: the flow becomes three dimensional. The Fourier mode  $m = 2$  grows exponentially, saturates at  $t = 20\,000 \text{ s}$  and reaches a steady state at  $t = 30\,000 \text{ s}$ . For  $J = 10 \text{ A m}^{-2}$ , a Hopf-like bifurcation has occurred: the mode  $m = 2$  remains dominant but the flow periodically oscillates. For  $J = 50 \text{ A m}^{-2}$ , the transition to 3-D turbulence has occurred. Although the flow exhibits large 3-D fluctuations, the axisymmetric Fourier component  $u_0$  remains dominant.

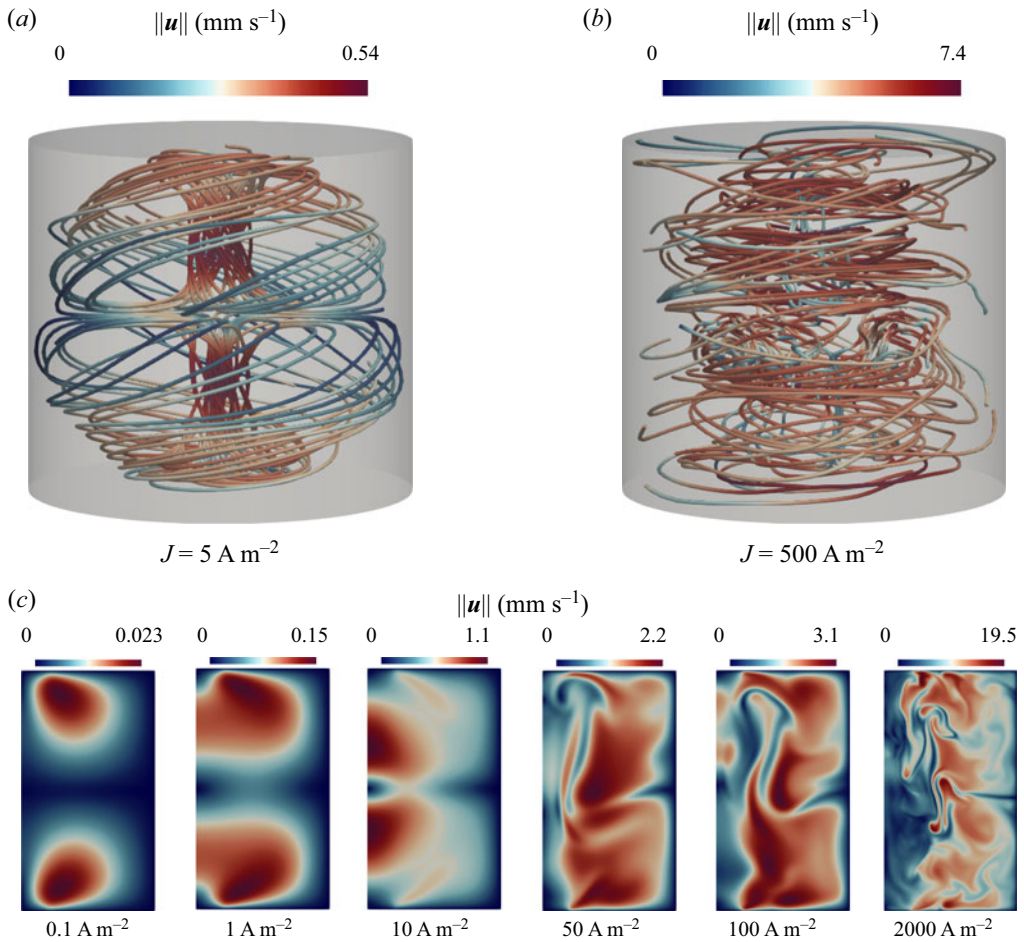


Figure 3. Variable  $J$ , axisymmetric simulations. Spatial structure of the flow. (a,b) Streamlines coloured by the velocity magnitude in axisymmetric simulations for different values of  $J$ . (c) Transition of the axisymmetric flow as  $J$  increases, visualized by the velocity magnitude  $\|\mathbf{u}\|$  in the meridian plane.

In figure 6(a) we show the time- and volume-averaged velocity  $\bar{u}_{3D}$  of these 3-D simulations. For comparison, we also show in this graph the time- and volume-averaged velocity obtained in axisymmetric simulations; we use the symbol  $\bar{u}_{axi}$  to differentiate it from the 3-D velocity. Inspection of the graph reveals that three dimensionalization appears between  $J = 1$  and  $5 \text{ A m}^{-2}$ . For high current densities, we observe  $\bar{u} \sim J^{1/2}$  or  $J^{5/9}$ . A fit of the curve on the three last points gives a slope of 0.51 for the axisymmetric simulations, which corresponds to the law  $\bar{u}_{axi} \sim J^{1/2}$ , and 0.55 for the 3-D ones, which corresponds rather to  $\bar{u}_{3D} \sim J^{5/9}$ . For medium current densities, the power law  $\bar{u} \sim J^{2/3}$  is not incompatible with the data, but we cannot say that this scaling regime is clearly visible.

We also note that the value of  $\bar{u}_{3D}$  is just slightly below  $\bar{u}_{axi}$ , obtained assuming axisymmetry. This is also visible in figure 6(b) where we plot the ratio  $\bar{u}_{3D}/\bar{u}_{axi}$  as a function of  $J$ . The flow is axisymmetric for very small values of the current (i.e.  $\bar{u}_{3D} = \bar{u}_{axi}$ ). The ratio  $\bar{u}_{3D}/\bar{u}_{axi}$  decreases as  $J$  grows up to the value  $J = 50 \text{ A m}^{-2}$ , after which the ratio fluctuates around 0.8.



Simulations of swirling electrovortex flows in cylinders

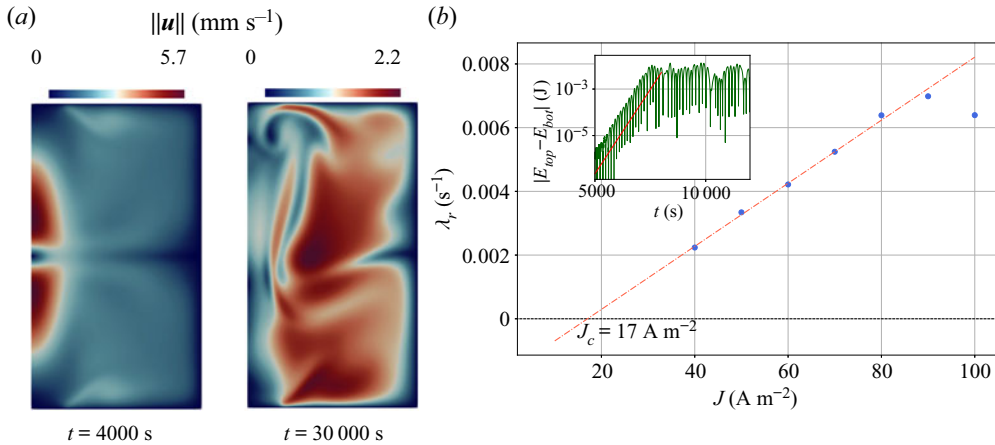


Figure 4. Variable  $J$ , axisymmetric simulations. First bifurcation of the flow. (a) The  $\|u\|$  structure before and after the first bifurcation for  $J = 50 \text{ A m}^{-2}$ . (b) Growth rate  $\lambda$  of the first axisymmetric instability as a function of  $J$  and extrapolated threshold  $J_c^{axi} = 17 \text{ A m}^{-2}$ . We measure the growth rate  $\lambda$  from the time series for  $|E_{top} - E_{bot}|$ , the difference in kinetic energy between the top and bottom half of the fluid domain.

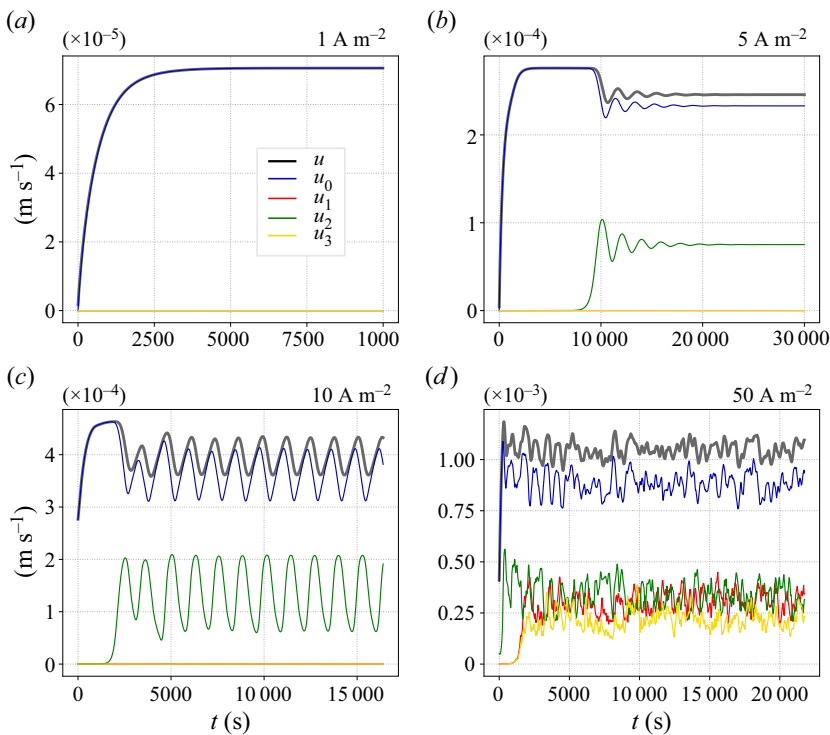


Figure 5. Variable  $J$ , 3-D simulations,  $M = 20$ . Time series of  $u$  and modal content  $u_0, u_1, u_2, u_3$  for different current densities  $J$  as marked in the figures.

We show snapshots of the spatial organisation of the flow in figure 7 for the following three values of the current  $J = 5, 50, 500 \text{ A m}^{-2}$ . The flow is clearly three dimensional. This figure shows the value of  $\|u\|$  in a meridian plane and in the horizontal plane located at  $z = 8.8 \text{ cm}$ . We observe that, for  $J = 5 \text{ A m}^{-2}$ , the equatorial symmetry by reflection is broken (there is a slight asymmetry between the lower and the upper half of the cell).

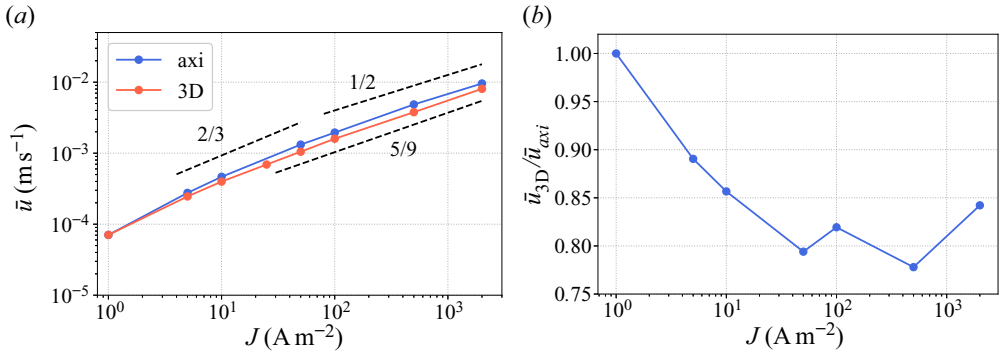


Figure 6. Variable  $J$ , 3-D simulations,  $M = 20$ . (a) Variation of  $\bar{u}$  with  $J$  in axisymmetrical and 3-D simulations. (b) Ratio  $\bar{u}_{3D}/\bar{u}_{axi}$  as a function of  $J$ .

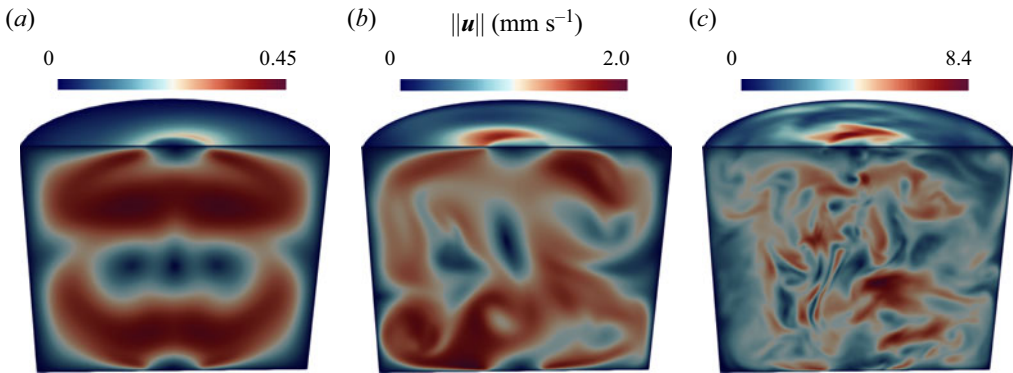


Figure 7. Variable  $J$ , 3-D simulations,  $M = 20$ . Spatial structure of the flow:  $\|u\|$  for  $J = 5, 50, 500 \text{ A m}^{-2}$ . The flow is steady for  $J = 5 \text{ A m}^{-2}$  and turbulent for  $J = 50, 500 \text{ A m}^{-2}$ . Results are shown for (a)  $J = 5 \text{ A m}^{-2}$ , (b)  $J = 50 \text{ A m}^{-2}$  and (c)  $J = 500 \text{ A m}^{-2}$ .

Recall that the flow is time independent though. The flows for  $J = 50 \text{ A m}^{-2}$  and  $J = 500 \text{ A m}^{-2}$  are clearly turbulent. The large- and small-scale structures seem to be equally distributed throughout the domain. The low-speed region near the axis that is observed in the axisymmetric simulations for large values of  $J$  (see figure 3c) is not present in these 3-D simulations.

Because of the large fluctuations of the flow for high current densities, we can wonder if 20 modes are enough to properly represent the flow. For this reason, we have done a small convergence study varying the number of Fourier modes  $M = 20$  to  $M = 40$  and for increasing  $J = 100, 500$  and  $2000 \text{ A m}^{-2}$ . On figure 8 we represent the time- and space-averaged modal kinetic energy  $E_c$  as a function of  $m$  for  $M = 20$  and  $M = 40$ . For  $J = 100 \text{ A m}^{-2}$ , the spectra show small differences above  $m \geq 15$ . For  $J = 500 \text{ A m}^{-2}$ , we find similar differences from  $m \geq 10$ . In both simulations the most energetic modes are well converged and, hence, we can limit resolution to  $M = 20$ . For  $J = 2000 \text{ A m}^{-2}$ , the spectra present more significant differences. The use of 40 modes is advisable in this case, since the azimuthal small scales are better resolved and certainly if the purpose is to access the fine turbulent structure of the flow. For the averaged velocity  $\bar{u}$  however, 20 or

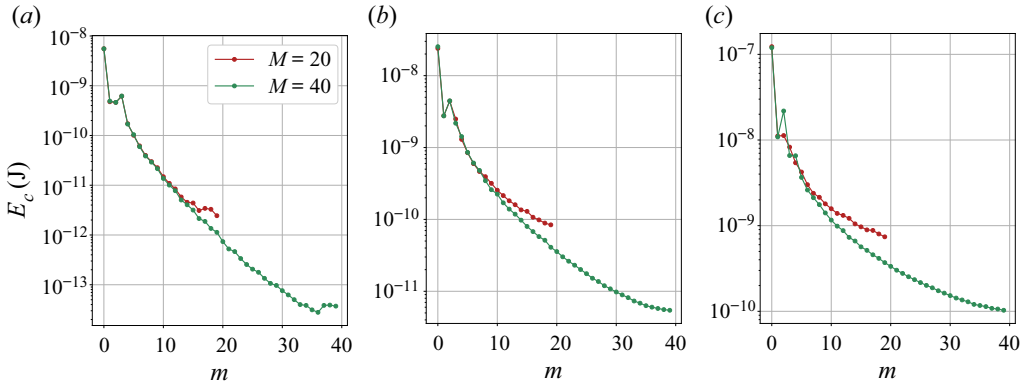


Figure 8. Variable  $J$ , 3-D simulations. Spectra of the kinetic energy averaged on time in the statistically steady state as a function of  $m$  for  $J = 100, 500, 2000 \text{ A m}^{-2}$  and  $M = 20$  and  $M = 40$ . The spectra show that 20 modes are sufficient for  $J = 100$  and  $J = 500 \text{ A m}^{-2}$ , but for  $J = 2000 \text{ A m}^{-2}$ , 40 modes are necessary to represent properly the first modes. Results are shown for (a)  $J = 100 \text{ A m}^{-2}$ , (b)  $J = 500 \text{ A m}^{-2}$  and (c)  $J = 2000 \text{ A m}^{-2}$ .

40 modes yield the same result. The plots of figure 6 obtained with  $M = 20$  remain valid up the highest value of  $J$ .

In figure 9(a) we focus our attention on the steady state and 3-D flow obtained with  $J = 5 \text{ A m}^{-2}$ . Recall that this value of the current is above the critical threshold for which the axisymmetry is broken. We display in this figure several representations of the flow structure. Note that the flow organisation is strikingly similar to that observed in the von Kármán flows described in Nore *et al.* (2003). We observe that the 3-D flow is also  $R_\pi$  symmetric (see (3.1)). The predominance of the Fourier mode  $m = 2$  is the spectral manifestation of the presence of two vortices roughly localized on the equatorial plane, rotating in the same direction, and with axes aligned with the directions  $\{\theta = -\pi/2, z = 0\}$  and  $\{\theta = \pi/2, z = 0\}$ . The centre of one vortex is visible between the two red/orange oblong structures in the right panel in figure 9(c). The vortices are separated by a transition layer that is oblong, roughly localized on the equatorial plane and slightly twisted. This transition layer is materialised in the centre and the right panels in figure 9(c) by blue regions. The numerical simulations indicate that the 3-D steady state undergoes a second bifurcation in the interval  $J \in [5, 10] \text{ A m}^{-2}$ . Beyond the critical value, the flow starts oscillating periodically, but the overall structure of the flow stays  $R_\pi$  symmetric. The reader is invited to watch the video provided in the supplementary movie available at <https://doi.org/10.1017/jfm.2022.779> to better appreciate the nature of this periodic flow. The simulation corresponding to the video is done with  $J = 10 \text{ A m}^{-2}$ .

A third bifurcation breaking the  $R_\pi$  symmetry occurs in the interval  $J = [10, 50] \text{ A m}^{-2}$ . Increasing the value of the current beyond this point quickly leads to a fully turbulent flow; see figure 7(c).

We determine the threshold of the first bifurcation (which we recall breaks the axisymmetry) by inspecting the time evolution of the modal volume-averaged values  $u_m$  for  $m = 1, 2, 3$ . Beyond the bifurcation threshold, some of these quantities start to grow exponentially. For instance, the inset of figure 10 shows that the Fourier components  $u_1$  and  $u_2$  grow exponentially in time. This technique allows us to measure the growth rates  $\lambda$  of the modes  $m = 1, 2$  for  $J = 1, 5, 10 \text{ A m}^{-2}$ . By linear fit we obtain  $J_c^{3D} \approx 2.5 \text{ A m}^{-2}$  for both modes  $m = 1$  and  $m = 2$ . A similar observation was made for the first bifurcation

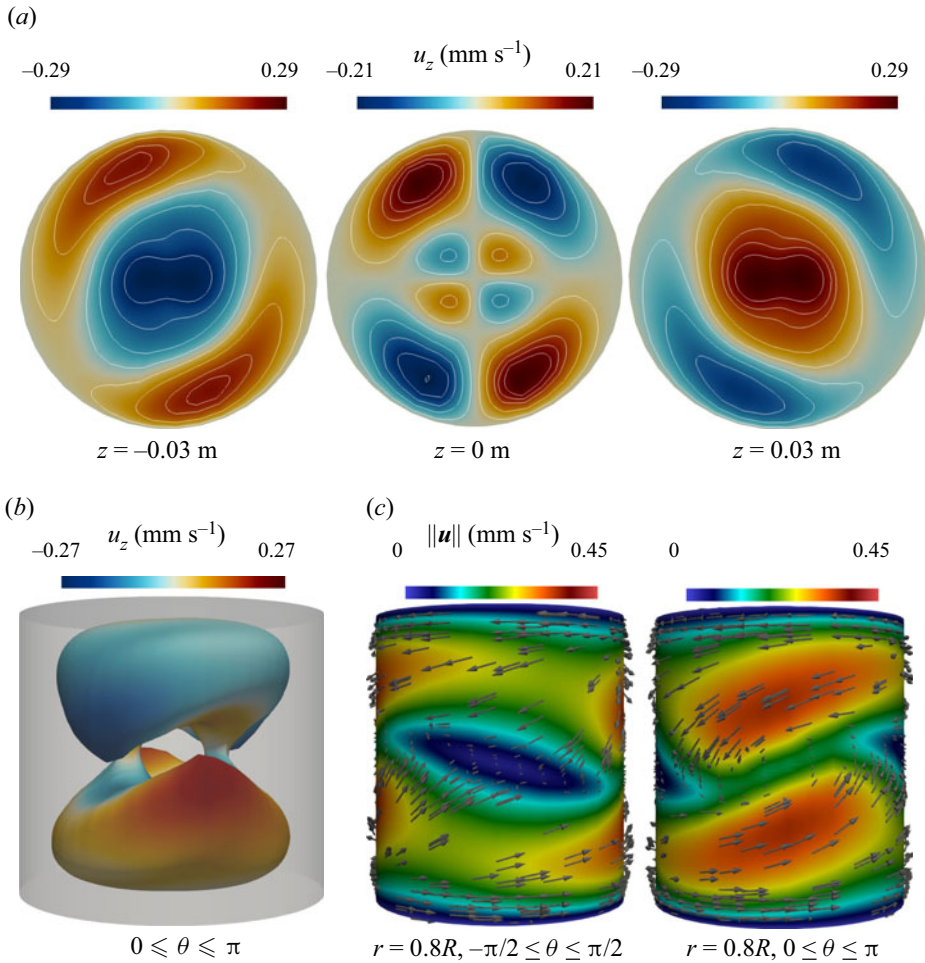


Figure 9. Variable  $J$ , 3-D simulations,  $M = 20$ . Flow after the first bifurcation for  $J = 5 \text{ A m}^{-2}$ . (a) Snapshots of  $u_z$  at  $z = -0.03 \text{ m}$ ,  $z = 0 \text{ m}$  and  $z = 0.03 \text{ m}$ . (b) Contour of  $\|\mathbf{u}\|$  taken for  $\|\mathbf{u}\| = 0.6 \|\mathbf{u}\|_{max}$  coloured by  $u_z$ . (c) Snapshots of  $\|\mathbf{u}\|$  at  $r = 0.8R$  for  $-\pi/2 \leq \theta \leq \pi/2$  (left) and  $0 \leq \theta \leq \pi$  (right). One sees the  $R_\pi$  symmetry and the dominance of the  $m = 2$  azimuthal mode: there are two opposite vortices and two opposite aspiration fronts, where the flow is directed towards the centre of the cylinder.

of the von Kármán flow reported in Nore *et al.* (2004), where there is also a bifurcation of codimension two (the aspect ratio is  $H/R \approx 1.64$  therein).

### 3.3. Variable $B$ , axisymmetric study

We now report the results obtained for a second series of numerical simulations where we investigate the influence of the magnitude of the imposed magnetic field. We use the same geometry of the cell as above, we fix  $J = 50 \text{ A m}^{-2}$ , and we use  $\nu = 3.2 \times 10^{-7} \text{ m}^2 \text{ s}^{-1}$ . Most simulations are done assuming axisymmetry. We have done one 3-D simulation at high field  $B = 10^{-1} \text{ T}$  with  $M = 20$  modes. The other numerical parameters used for the simulations are reported in table 2.

We show in figure 11 the time- and volume-averaged velocity,  $\bar{u}$ , as a function of  $B$ . We observe that the behaviour of  $\bar{u}$  is not monotone with respect to  $B$ :  $\bar{u}$  first increases with

Simulations of swirling electrovortex flows in cylinders

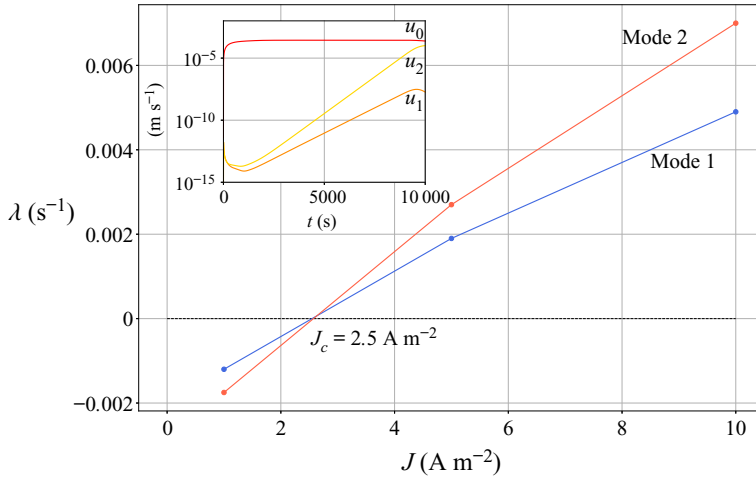


Figure 10. Variable  $J$ , 3-D simulations,  $M = 20$ . Threshold of the first bifurcation in three dimensions. Beyond a certain current density we observe exponential growth on  $u_1$  and  $u_2$ , as shown in the inset at  $J = 5 \text{ A m}^{-2}$ . The measured growth rates allow us to locate the threshold of the first 3-D bifurcation near  $J_c^{3D} \approx 2.5 \text{ A m}^{-2}$  for both modes  $m = 1, 2$ .

$B$ (T)	$\Delta l$ (m)	$\Delta t$ (s)	$\overline{Re}$	$\overline{\Gamma}$
$5 \times 10^{-5}$	0.0025 $\rightarrow$ 0.005	$5 \times 10^{-2}$	52	$5.4 \times 10^{-4}$
$1 \times 10^{-4}$	0.0025 $\rightarrow$ 0.005	$5 \times 10^{-2}$	90	$1.9 \times 10^{-3}$
$2 \times 10^{-4}$	0.0025 $\rightarrow$ 0.005	$2 \times 10^{-2}$	149	$6.2 \times 10^{-3}$
$5 \times 10^{-4}$	0.0025 $\rightarrow$ 0.005	$2 \times 10^{-2}$	287	$3.0 \times 10^{-2}$
$1 \times 10^{-3}$	0.0025 $\rightarrow$ 0.005	$4 \times 10^{-2}$	409	$8.6 \times 10^{-2}$
$2 \times 10^{-3}$	0.0005 $\rightarrow$ 0.0025	$5 \times 10^{-3}$	594	$2.5 \times 10^{-1}$
$1 \times 10^{-2}$	0.0005 $\rightarrow$ 0.0025	$1 \times 10^{-3}$	858	1.8
$5 \times 10^{-2}$	0.0005 $\rightarrow$ 0.0025	$1 \times 10^{-3}$	716	7.5
$1 \times 10^{-1}$	0.0005 $\rightarrow$ 0.0025	$1 \times 10^{-3}$	521	11
$5 \times 10^{-1}$	0.0005 $\rightarrow$ 0.0025	$1 \times 10^{-4}$	105	11
1	0.001 $\rightarrow$ 0.005	$5 \times 10^{-5}$	52	11

Table 2. Numerical parameters for the axisymmetric simulations with variable  $B$ . Mesh size  $\Delta l$  (non-uniform meshes, smallest  $\rightarrow$  largest mesh size), time step  $\Delta t$ , non-dimensional numbers  $\overline{Re} = \overline{u}R/\nu$  and  $\overline{\Gamma} = \sigma \overline{u}B/J$ .

$\nu$ ( $\text{m}^2 \text{ s}^{-1}$ )	$\Delta l$ (m)	$\Delta t$ (s)	$\overline{Re}$	$\overline{\Gamma}$
$3.2 \times 10^{-5}$	0.0025 $\rightarrow$ 0.005	$5 \times 10^{-2}$	0.14	0.0030
$8.1 \times 10^{-6}$	0.0025 $\rightarrow$ 0.005	$2 \times 10^{-2}$	2.3	0.012
$1.3 \times 10^{-6}$	0.0025 $\rightarrow$ 0.005	$2 \times 10^{-2}$	62	0.051
$5 \times 10^{-7}$	0.0025 $\rightarrow$ 0.005	$1 \times 10^{-2}$	250	0.081
$3.2 \times 10^{-7}$	0.0025 $\rightarrow$ 0.005	$4 \times 10^{-2}$	409	0.086
$8.1 \times 10^{-8}$	0.0025 $\rightarrow$ 0.005	$5 \times 10^{-3}$	1892	0.1

Table 3. Numerical parameters for the axisymmetric simulations with variable  $\nu$ . Mesh size  $\Delta l$  (non-uniform meshes, smallest  $\rightarrow$  largest mesh size), time step  $\Delta t$ , non-dimensional numbers  $\overline{Re} = \overline{u}R/\nu$  and  $\overline{\Gamma} = \sigma \overline{u}B/J$ .

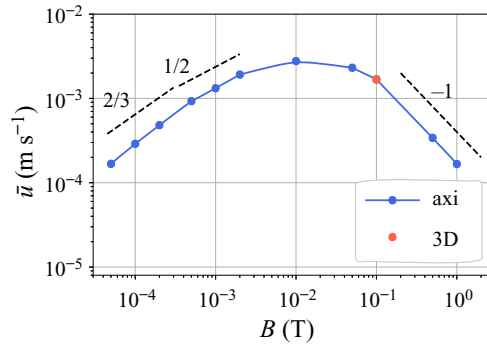


Figure 11. Variable  $B$ , axisymmetric simulations. The typical flow magnitude  $\bar{u}$  first increases with the magnetic field  $B$ , but decreases back again for very intense imposed magnetic fields.

$B$  and then sharply decays above a certain magnetic field strength. Power laws  $\bar{u} \sim B^{2/3}$  followed by  $\bar{u} \sim B^{1/2}$  and later  $\bar{u} \sim B^{-1}$  are observed as  $B$  increases.

Figure 12 shows snapshots of the magnitude of the electrical current density  $\|\mathbf{j}\|$  and the magnitude of the velocity  $\|\mathbf{u}\|$  for three values of the magnitude of the imposed magnetic field:  $B = 10^{-3}, 10^{-2}, 10^{-1}$  T. In each panel of figure 12 the electrical current density is shown on the left and the magnitude of the velocity is shown on the right. We observe that the flow becomes steady as  $B$  increases. For the largest value of  $B$ , we observe that the current density and the fluid motion are localised in a thin vertical cylinder whose two extremities coincide with the contact surfaces with the two wires supplying and extracting the current. In this case the flow is axisymmetric. We ran a 3-D simulation for  $B = 10^{-1}$  T. The volume-averaged velocity  $\bar{u}$  is the same in both axisymmetric and 3-D simulations (red point in figure 11), and the 3-D modes ( $m \neq 0$ ) are zero. It seems that high  $B$  makes the flow more axisymmetric. The reorganisation of the current density distribution in the cell and the drastic reduction of the fluid motion are due to the induction effects generated by the term  $\sigma \mathbf{u} \times B \mathbf{e}_z$  in (2.1b).

Note also that we do not observe any Shercliff or Hartmann boundary layers at high magnetic field as in duct flows (Hunt & Stewartson 1965; Moresco & Alboussiere 2004) in this set-up. Such layers are always localised near the solid boundaries of the domain and channel the electrical current when the Hartmann number

$$Ha = BR \left( \frac{\sigma}{\rho \nu} \right)^{1/2} \quad (3.2)$$

is large. Here  $Ha \approx 4, 40, 400$  for the three simulations reported in figure 12, and does increase from left to right. But in our case the current density and imposed magnetic field are roughly parallel whereas they are perpendicular in the case of duct flows.

### 3.4. Variable $\nu$ , axisymmetric study

We now explore the influence of the viscosity. We fix  $J = 50 \text{ A m}^{-2}$ ,  $B = 1 \text{ mT}$ , and we artificially vary the viscosity  $\nu$  of the liquid metal. Usually, the viscosity of a liquid metal is between  $10^{-7}$  and  $10^{-6} \text{ m}^2 \text{ s}^{-1}$ , but we extend the study to other non-realistic viscosities in order to better understand the flow's behaviour. Only axisymmetric simulations are done. The other numerical parameters used for the simulations are reported in table 3. We focus our attention on the influence of the viscosity on the time- and volume-averaged velocity,  $\bar{u}$ . The results of these simulations in the range  $\nu \in [8 \times 10^{-8}, 3 \times 10^{-5}] \text{ m}^2 \text{ s}^{-1}$  are shown

## Simulations of swirling electrovortex flows in cylinders

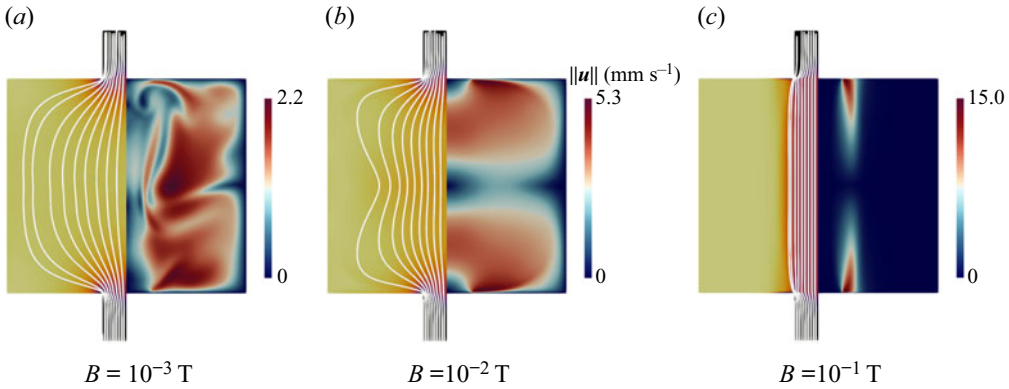


Figure 12. Variable  $B$ , axisymmetric simulations,  $J = 50 \text{ A m}^{-2}$ . The spatial structure of the current density (left) and of the magnitude of the velocity (right) varies significantly when the intensity of the magnetic field increases. For the lowest value of  $B$ , the flow is turbulent and the current density is barely influenced by inductive effects ( $\sigma \mathbf{u} \times B \mathbf{e}_z$ ). For the largest value of  $B$ , the induction effects are strong. The flow becomes steady and due to the induction effects the electrical current almost goes in straight lines from the top wire to the bottom wire. The current density is scaled from yellow to purple in the range  $[0, J_w]$ , where  $J_w = 1250 \text{ A m}^{-2}$  is the imposed current density in the wires.

in figure 13. For small values of the viscosity, it seems that  $\bar{u} \sim \nu^{-1/9}$  or  $\nu^0$  as in (1.2). When the viscosity is large, we observe  $\bar{u} \sim \nu^{-1}$ , which is a clear indication of the Stokes regime.

### 3.5. One master curve for the intensity of flow in the inductionless regime

We have deliberately chosen in the previous sections to report all the results in dimensional form to make clear that the effects of increasing  $J$  and increasing  $B$  are not always equivalent. This difference is mainly due to inductive effects. If  $U$  is a typical velocity, we can estimate that induction is not important as long as

$$\Pi = \frac{\sigma UB}{J} \ll 1. \quad (3.3)$$

In this inductionless regime, we can group all our previous measures of flow intensity using a non-dimensional representation. A natural scale for velocity in the inertial regime is  $(JB R/\rho)^{1/2}$  and with it, we can define a Reynolds number as

$$Re_{in} = \left( \frac{JB}{\rho} \right)^{1/2} \frac{R^{3/2}}{\nu}, \quad (3.4)$$

which only depends on input parameters (hence, subscript *in*). In figure 14 we plot  $\bar{Re} = \bar{u}R/\nu$ , the Reynolds number based on the measured velocity as a function of  $Re_{in}$  for the axisymmetric simulations that meet the requirement (3.3) (we only take the data in the range  $B \in [0, 2]$  mT for the simulations with varying  $B$ ). It is remarkable that all the data points collapse on a single curve. At high  $Re_{in}$ , we observe not unexpectedly that  $\bar{Re} \sim Re_{in}$ .

### 3.6. Scaling laws for swirling EVFs

All our simulations were done in the limit  $\Gamma = \mu_0 J R/B \ll 1$ , where the EVF always has a strong swirling character. Here we explain the different scaling regimes of such swirling

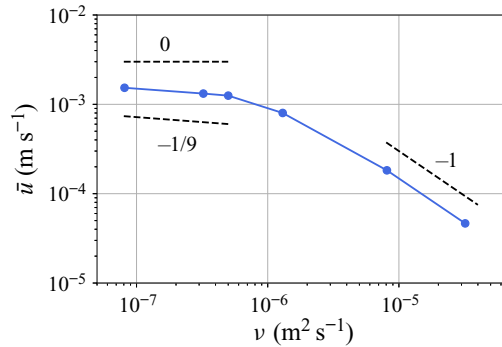


Figure 13. Variable  $\nu$ , axisymmetric simulations. Velocity  $\bar{u}$  as a function of the viscosity  $\nu$ . The slope asymptotes between 0 and  $-1/9$  for low viscosities and to  $-1$  for high viscosities.

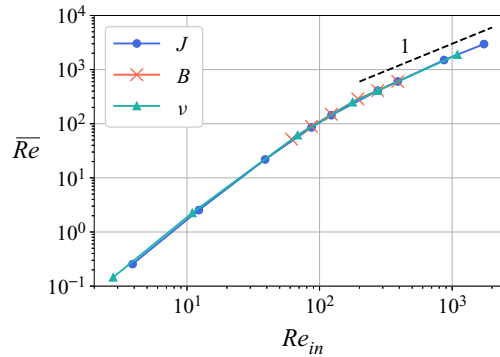


Figure 14. Computed Reynolds number  $\bar{Re} = \bar{u}R/\nu$  as a function of input parameter Reynolds numbers  $Re_{in}$  defined in (3.4).

EVFs. We introduce  $[\mathbf{u}] = U$ ,  $[\mathbf{j}] = J$  and  $[\mathbf{b}] = B$  as typical scales of velocity, current density and magnetic field.

We start with the large  $B$ , inductive regime. When induction, i.e. the term  $(\sigma \mathbf{u} \times \mathbf{b})$ , is important in Ohm's law, the Lorentz force acts as a magnetic brake on the bulk flow (Hunt & Malcolm 1968). We conjecture that saturation of flow magnitude occurs when this bulk magnetic braking balances the inductionless part of the Lorentz force with magnitude  $JB$ . This balance implies that

$$U \sim \frac{J}{\sigma B} \quad (\text{inductive}) \quad (3.5)$$

or  $\Pi \sim 1$ . This scaling law is coherent with what we observed at high  $B$ .

When induction is not important, when  $\Pi \ll 1$ , we can imagine three possible regimes: viscous, intermediate and inertial. For very weak Lorentz forces, the Lorentz force can be balanced by the viscous forces,  $[\rho \nu \nabla^2 \mathbf{u}] \sim [\mathbf{j} \times \mathbf{b}]$ . In this Stokes regime the flow occupies the entire cell, so we can use  $[\mathbf{r}] = R$  as the length scale. From this balance we then find that

$$U \sim \frac{JBR^2}{\rho \nu}, \quad (\text{inductionless, viscous}). \quad (3.6)$$



This viscous regime was clearly visible in our simulations when the flow speed was at its lowest.

For the highest flow intensities, inertia will be dominant in opposing the Lorentz force. Naively speaking, we can simply balance  $[\rho(\mathbf{u} \cdot \nabla)\mathbf{u}] \sim [\mathbf{j} \times \mathbf{b}]$  and, using somewhat arbitrarily  $[\mathbf{r}] = R$  as the length scale, we then find that

$$U \sim \left(\frac{JBR}{\rho}\right)^{1/2}, \quad (\text{inductionless, inertial } 1/2). \quad (3.7)$$

A more elaborate analysis of the torque balance between the boundary and the bulk (Davidson 1992; Davidson *et al.* 1999) yields

$$U \sim \left(\frac{JBR}{\rho}\right)^{5/9} \left(\frac{R}{\nu}\right)^{1/9}, \quad (\text{inductionless, inertial } 5/9). \quad (3.8)$$

The inertial regime was clearly visible in our simulations, but we cannot conclude which exponent, 1/2 or 5/9, is more adapted.

An intermediate regime can sometimes be observed when the viscous effects, the inertial effects and the Lorentz force are all of the same intensity. This is possible because forcing mainly occurs near the electrical contact, in the viscous boundary layer. The scaling law for this intermediate regime is derived in Herreman *et al.* (2021). Using the  $z$  component of the vorticity equation, the three-term balance requires that  $[(\mathbf{u} \cdot \nabla)\omega_z - (\boldsymbol{\omega} \cdot \nabla)u_z] \sim [\rho^{-1}B\partial_z j_z] \sim [\nu\partial_{zz}^2\omega_z]$ . In a boundary layer of width  $\delta$  near the electrical contacts with the wires, we estimate  $[\partial_z] = \delta^{-1}$  and  $[\partial_r] = R^{-1}$ . If  $[u_r, u_\theta] = U$  then  $[u_z] = U\delta R^{-1}$  due to incompressibility. This yields the estimates  $[\omega_r, \omega_\theta] = U\delta^{-1}$  and  $[\omega_z] = UR^{-1}$  for the vorticity. Inserting these scales in the three-term balance, we obtain two equivalence relations  $U^2/R^2 \sim JB/\rho\delta \sim \nu U/R\delta^2$ , from which, after eliminating  $\delta$ , we find that

$$U \sim \left(\frac{JB}{\rho}\right)^{2/3} \frac{R}{\nu^{1/3}}, \quad (\text{inductionless, laminar boundary layer}), \quad (3.9)$$

where the power law  $U \sim J^{2/3}$  was clearly visible in the simulations of Herreman *et al.* (2021), it is much less visible in the present set-up. We think that this may be due to the fact that the von Kármán-like flow, driven here, is rather unstable and easily turbulent in the bulk. If turbulent flow structures reach into the boundary layer, the latter will no longer remain laminar and this will break the subtle three-term balance. In Appendix A we show that the 2/3 scaling can also be derived from the model of Davidson (1992), if one uses a laminar friction law for the viscous stress, which is equivalent to supposing a laminar boundary layer.

#### 4. Geometrical influences on a swirling EVF

In this section we investigate the influence of the geometry of the cell and of the connecting wires on the fluid flow.

We examine the influence of  $R_w$ , the wire radius, the influence of  $H$ , the cell's height and the impact of using asymmetrical wires as in Herreman *et al.* (2021). All the simulations are done with the magnetic field magnitude  $B = 1$  mT and with realistic viscosity  $\nu = 3.23 \times 10^{-7} \text{ m}^2 \text{ s}^{-1}$ .

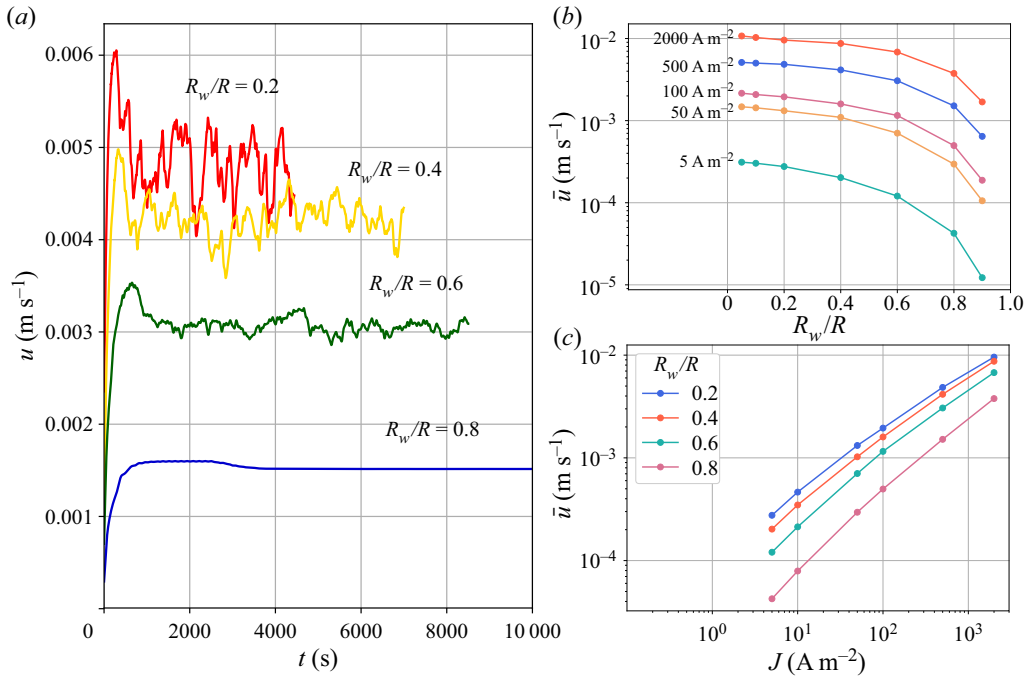


Figure 15. Variable  $R_w$ , axisymmetric simulations. Global measures. (a) Time series of the velocity  $u$  for different  $R_w/R$  and  $J = 500 \text{ A m}^{-2}$ . Plot of  $\bar{u}$  as (b) a function of  $R_w/R$  for different  $J$ , and (c) a function of  $J$  for different  $R_w/R$ . The mean velocity increases with  $J$  and decreases with  $R_w/R$  and all curves present similar trends.

#### 4.1. Variable wire radius $R_w$

As in § 3, we fix the geometry of the cell to be  $(R, H, H_w) = (10, 18, 4)$  cm and vary both the radius  $R_w$  of the connecting wires and the current density  $J$ . We expect the intensity of the fluid flow generated by the electrovortex to be a decreasing function of the ratio  $R_w/R$  (Bojarevičs *et al.* 1989).

We show in figure 15(a) the space-averaged velocity  $u$  as a function of time for the following four values of the ratio  $R_w/R$ : 0.2, 0.4, 0.6, 0.8, and with  $J = 500 \text{ A m}^{-2}$ . These simulations are done assuming axisymmetry. As expected, both the time average of  $u$  and the time fluctuations of  $u$  increase as the ratio  $R_w/R$  decreases. In figure 15(b) we show  $\bar{u}$  as a function of  $R_w/R$  for the following five values of  $J$ : 5, 50, 100, 500, 2000  $\text{A m}^{-2}$ . In figure 15(c) we show  $u_{bar}$  as a function of  $J$  for the following four values of  $R_w/R$ : 0.2, 0.4, 0.6, 0.8. Here again, we observe that the flow intensity decreases monotonically as  $R_w/R$  increases. This observation holds for all the values of the current.

In figure 16 we show snapshots of  $\|\mathbf{u}\|$  for the following four values of the ratio  $R_w/R$ : 0.2, 0.4, 0.6, 0.8 with  $J = 500 \text{ A m}^{-2}$ . One axisymmetric and one fully 3-D simulation have been done for each value of  $R_w/R$ . Three-dimensional simulations have been computed with  $M = 20$ , as justified in § 3.2. In the axisymmetric simulations (top panels), we always observe a cylindrical region where the fluid is approximately at rest. The diameter of this cylindrical region coincides with that of the connecting wires. In the corresponding 3-D simulations (bottom panels), this low-speed cylindrical core is absent and the flow is overall more turbulent. The flow speed remains close to that of the axisymmetric simulations.

Simulations of swirling electrovortex flows in cylinders

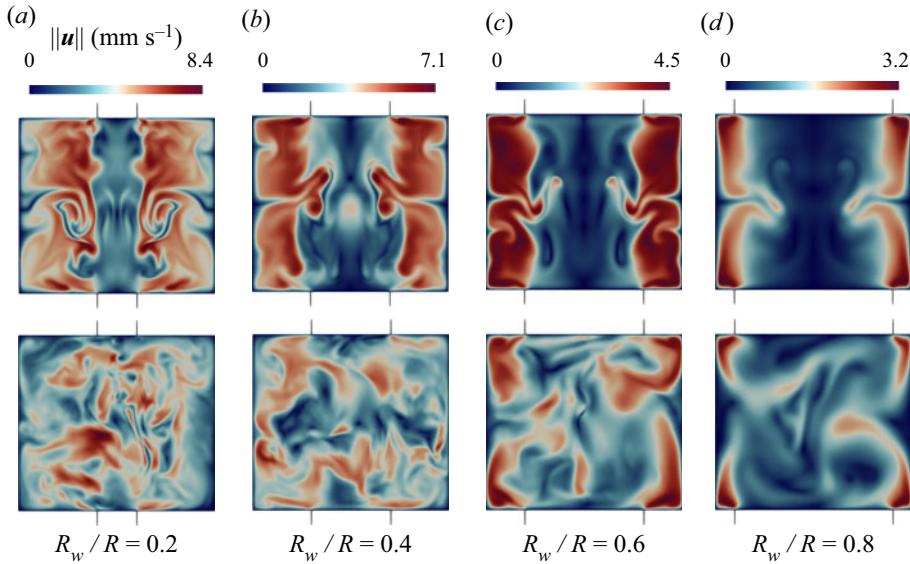


Figure 16. Variable  $R_w$ , axisymmetric and 3-D simulations. Snapshots of the velocity field  $\|\mathbf{u}\|$  for  $J = 500 \text{ A m}^{-2}$  and different  $R_w/R$ . Top row: axisymmetric simulations; bottom row: 3-D simulations. In axisymmetrical simulations we observe low speeds in a cylinder with radius  $R_w$ . In 3-D simulations such a low-speed region is less visible and turbulent structures are present everywhere.

It is tempting to try to model the dependence of the typical flow speed on  $R_w/R$ . For non-swirling EVFs ( $B = 0$ ), *ad hoc* fitting laws are given by Vlasjuk (1987) and Chudnovskii (1989) proposed a theoretical model based on a meridional contour integral. Unfortunately, one cannot generalize the method of Chudnovskii (1989) to swirling EVFs. In Appendix B we approximately calculate the torque that the Lorentz force exerts on the bottom half of the fluid domain and how it depends on  $R_w$ . This calculation requires  $b_\theta$  right above the electrical contact and we use the  $b_\theta$  profile that is observed with Millere boundary conditions (Millere *et al.* 1980; Herreman *et al.* 2019) or above a uniform current inlet. This yields torques

$$K = K_0 \begin{cases} 1 - (4R_w^2/3R^2) & \text{(Millere),} \\ 1 - R_w^2/R^2 & \text{(uniform),} \end{cases} \quad (4.1)$$

with  $K_0 = \frac{1}{4}IBR^2$ . Both expressions give a parabolic decay of the torque as  $R_w/R$  increases. We compare in figure 17(a) these two expressions with the actual torque obtained from the numerical simulations. We observe that the model based on Millere's approximation is very accurate in the range  $R_w/R \in [0, 0.5]$ . We now estimate the dependence of the intensity of the flow motion,  $U$ , with respect to  $R_w/R$ , by assuming  $U$  is proportional to torques

$$U \approx U_0 \begin{cases} 1 - (4R_w^2/3R^2) & \text{(Millere),} \\ 1 - R_w^2/R^2 & \text{(uniform).} \end{cases} \quad (4.2)$$

Here  $U_0$  is the maximum of  $U$  in the limit  $R_w/R \rightarrow 0$ . We show in figure 17(b) the quantity  $\bar{u}/u_0$  as a function of  $R_w/R$ . We also show in this figure the two theoretical profiles  $1 - \alpha(R_w^2/R^2)$  with  $\alpha = 4/3$  and 1. We have estimated  $u_0$  by fitting the parabola

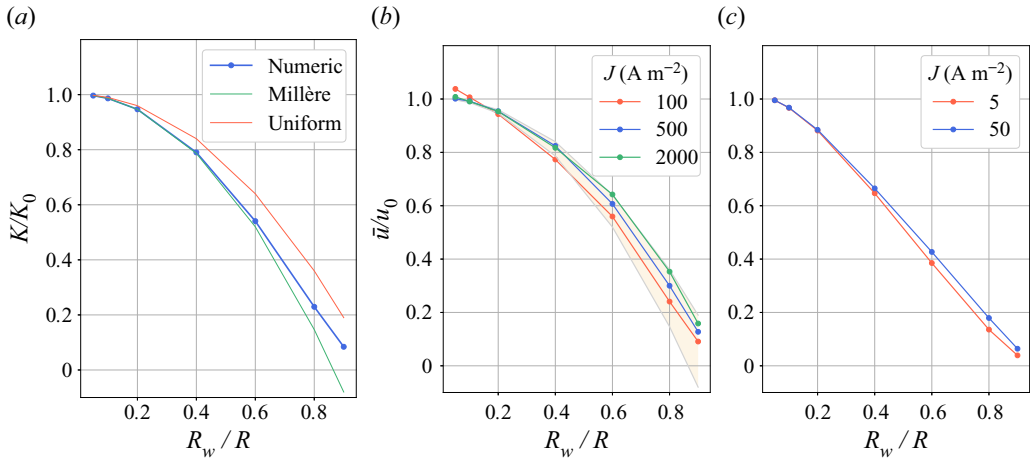


Figure 17. Model for the geometrical dependence of flow intensity on wire radius. (a) Normalized torque  $K/K_0$  as a function of  $R_w/R$ . The Millère model works really well for  $R/R_w < 0.6$ . (b) Normalized velocity  $\bar{u}/u_0$  as a function of  $R_w/R$  for high  $J$ . The orange zone corresponds to the zone between the two theoretical profiles, uniform and Millère. The fit of the velocity works well. (c) Normalized velocity  $\bar{u}/u_0$  for low  $J$ . A linear fit seems more accurate for these low current densities.

$\bar{u} = u_0(1 - \beta(R_w/R)^2)$  to the data shown in figure 15(b). This shows that the estimation of the velocity dependence on  $R_w/R$  can be quite accurate for intermediate  $J$ . However, we do observe that the parabolic profile does not fit very well the data when  $J$  is very small, a linear profile fits better the data in this limit (see figure 17c).

#### 4.2. Variable height $H$

Up until now, all simulations were done in a cell with aspect ratio  $H/R = 1.8$ . We now vary  $H/R$  and study how this affects the flow. We run axisymmetric simulations where we vary  $H$  for several values of the current density  $J$  and keep  $(R, R_w, H_w) = (10, 2, 4)$  cm.

In figure 18(a) we show the time history of the volume-averaged velocity observed in simulations done with the aspect ratios  $H/R = 0.5, 1.0, 1.8$  and with the current density  $J = 500 \text{ A m}^{-2}$ . We observe that the larger  $H/R$ , the larger  $u$  and the larger the fluctuations of  $u$ . In figure 18(b–c) we show the quantities  $\bar{u}$  and  $\bar{u}_{max}$  as functions of  $J$  for the three considered aspect ratios. The time- and space-averaged velocity scales like  $\bar{u} \sim J^{1/2}$  for large values of  $J$  for the three values of  $H/R$  investigated. The maximal speed  $\bar{u}_{max}$  behaves in a slightly different manner. We observe that  $\bar{u}_{max}$  is independent of  $H/R$  when  $J$  is large. The power law  $\bar{u}_{max} \sim J^{1/2}$  seems to apply when  $H/R$  is large, whereas the power law  $\bar{u}_{max} \sim J^{2/3}$  seems a better fit when  $H/R$  is small. With lower  $H/R$ , we observe that the flow is less turbulent (weaker oscillations are, for example, visible in figure 18(a) at  $H/R = 0.5$ ). This probably explains why the  $2/3$ , laminar boundary layer scaling law applies better in cylinders with a low aspect ratio  $H/R$ .

Figure 19 shows the spatial distribution of  $\|u\|$  in the meridian section for the two current densities  $J = 5, 500 \text{ A m}^{-2}$  and for the three aspect ratios  $H/R = 0.5, 1.0, 1.8$ . The flow is time independent for the smallest value of the current density  $J = 5 \text{ A m}^{-2}$ , but it is turbulent for the larger value  $J = 500 \text{ A m}^{-2}$ . When the aspect ratio is small, i.e.  $H/R = 0.5$ , the fluid motion is somewhat restricted to a small region close to the vertical axis.

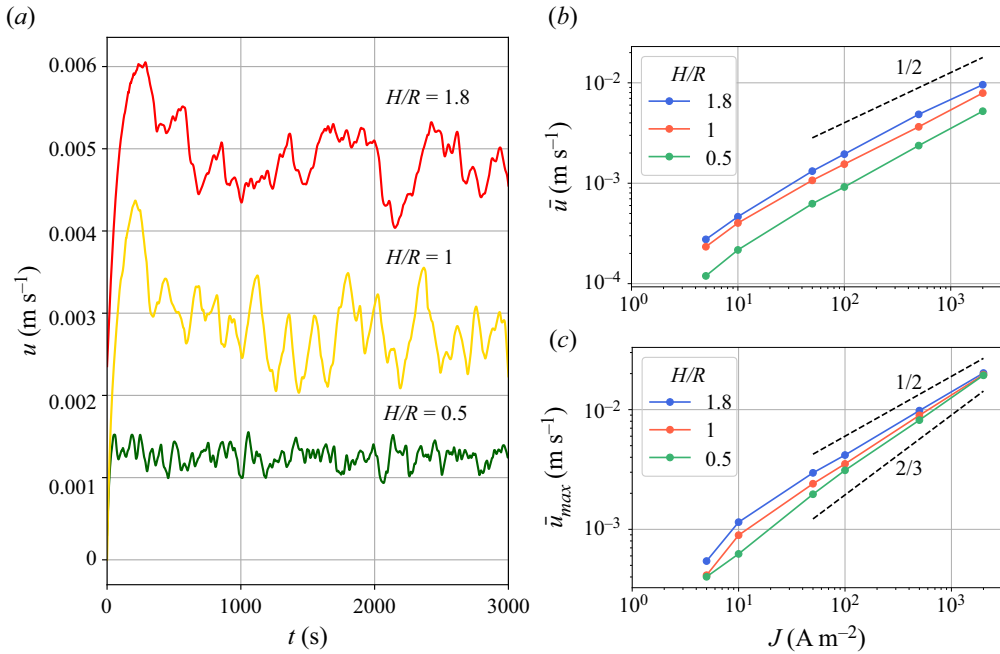


Figure 18. Variable  $H$ , axisymmetric simulations. (a) Time series of  $u$  for different aspect ratios and  $J = 500 \text{ A m}^{-2}$ . The higher the cell is, the more intense and fluctuating the flow is. Plots of (b)  $\bar{u}$  and (c)  $\bar{u}_{max}$  as a function of  $J$ . The scaling law  $1/2$  is observed for each aspect ratio for  $\bar{u}$ , but it changes when one looks at  $\bar{u}_{max}$ , where the scaling law  $2/3$  is better adapted to cells with a smaller aspect ratio.

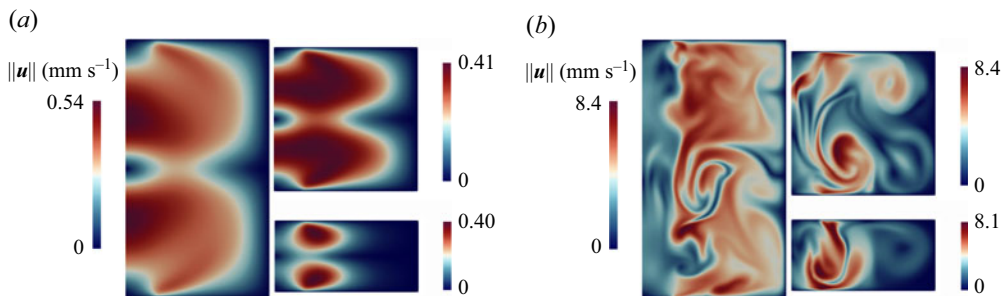


Figure 19. Variable  $H$ , axisymmetric simulations. Snapshots of  $\|\mathbf{u}\|$  for (a)  $J = 5 \text{ A m}^{-2}$  and (b)  $J = 500 \text{ A m}^{-2}$ . In cells with small aspect ratios, the flow does not reach the high  $r$  regions. The flow remains localized above and below the electrical contact.

This localisation will bias the spatial average in  $\bar{u}$  and this likely explains the difference in behaviour of  $\bar{u}$  and  $\bar{u}_{max}$  observed in figure 18(b-c).

#### 4.3. Symmetrical vs asymmetrical wires

In our set-up, current is injected and withdrawn using a symmetrical pair of wires with the same diameter  $R_w$ . This is different from the asymmetrical cell simulated in Herreman *et al.* (2021), that only has one thin wire extracting current at the bottom. We investigate the effect of this symmetrical or asymmetrical current injection by comparing two cells with different connections. We set  $R = 10 \text{ cm}$  for both cells. In the first cell we fix the aspect

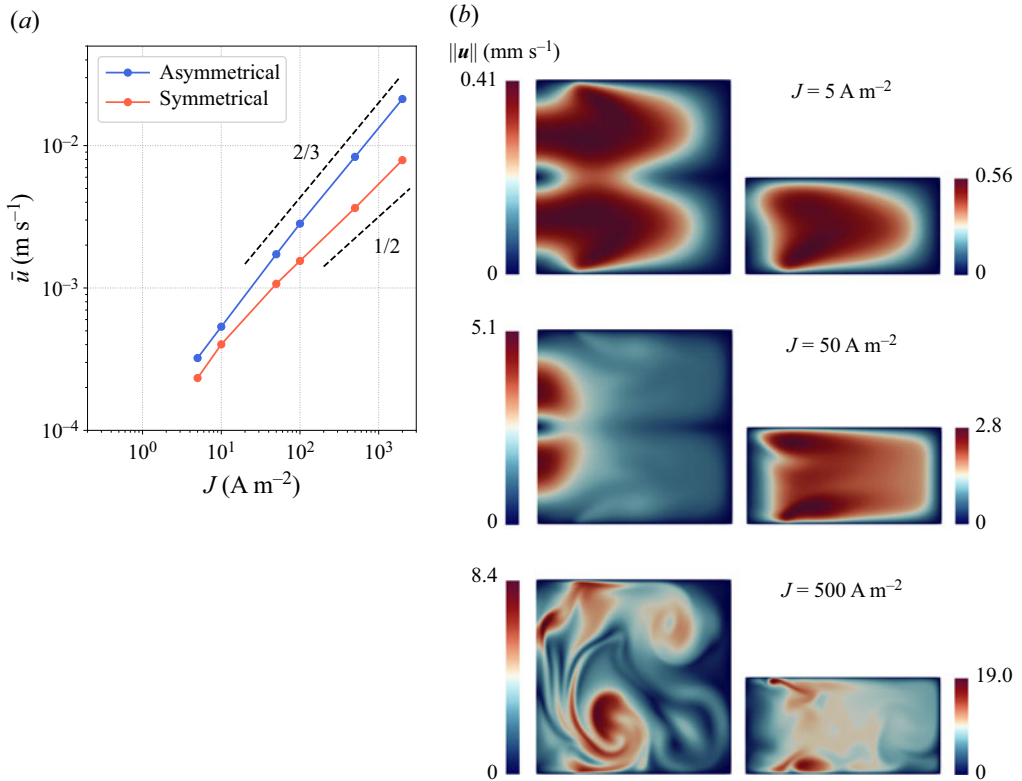


Figure 20. Symmetrical and asymmetrical set-ups. (a) Time- and space-averaged magnitude of the velocity  $\bar{u}$  as a function of  $J$  in both set-ups. (b) Snapshots of  $\|u\|$  in the symmetrical cell  $H/R = 1$  and the asymmetrical cell  $H/R = 0.5$ .

ratio to be  $H/R = 1$  and we use connecting wires at the top and bottom of the cell with the same radius and height  $(R_w, H_w) = (2, 4)$  cm. For the second cell, we set  $H/R = 0.5$  and we use only one thin wire at the bottom of the cell with  $(R_w, H_w) = (2, 4)$  cm. The current density is supposed uniform and equal to  $J$  at the top lid as in Herreman *et al.* (2021). All the simulations are axisymmetric. We fix  $B = 1$  mT and  $\nu = 3.2 \times 10^{-7} \text{ m}^2 \text{ s}^{-1}$ , and we vary  $J$ .

In figure 20(a) we show the typical velocity magnitude  $\bar{u}$  observed in the two configurations as a function of  $J$ . It appears that  $\bar{u}$  is significantly higher in the asymmetrical set-up than in the symmetrical one. For large values of the current, we observe that  $\bar{u} \sim J^{1/2}$  in the symmetrical set-up, but in the asymmetrical set-up we observe the laminar boundary layer scaling law,  $\bar{u} \sim J^{2/3}$ , just as in Herreman *et al.* (2021). This suggests that the flows are radically different in both configurations, so let us compare their spatial structure.

In figure 20(b) we compare snapshots of  $\|u\|$  in the asymmetrical and symmetrical set-ups for three values of  $J$ . At low  $J$ , the flows are quite comparable in both configurations. The only real difference is the velocity on the axis which is almost zero in the asymmetrical cell contrary to the symmetrical one. For higher  $J$ , there are significant differences in the flow structure. In the case  $J = 50 \text{ A m}^{-2}$ , the flow is localized near the axis in the symmetrical set-up, but fills the entire cell in the asymmetrical one. For  $J = 500 \text{ A m}^{-2}$ , the flow in the symmetrical cell has a vertical structure that is significantly

more turbulent. We think that this increased turbulence is due to the mixing layer that is present in the equatorial plane of the symmetrical set-up but is absent in the asymmetrical set-up. Such an equatorial mixing layer loses its stability fairly easily in von Kármán flows (Nore *et al.* 2003, 2004) and here this seems to be just the same. The 2/3 scaling regime likely requires a not too turbulent flow in the bulk.

### 5. Conclusion

In this paper we have characterized the fluid flow produced by the swirling electrovortex mechanism in a cylinder filled with GaInSn metal. Using axisymmetric and 3-D simulations, we have shown that, for a cylindrical container of aspect ratio  $H/R = 1.8$ , the flow thus produced shares many similarities with the von Kármán flow driven by two counter-rotating disks. Increasing  $J$  leads to a more intense flow and we observe a typical bifurcation sequence in 3-D simulations. First, the axisymmetry is broken in favour of an azimuthal mode  $m = 2$  with  $R_\pi$  symmetry. Secondly, there is a Hopf bifurcation and a time-dependent  $R_\pi$  symmetric state is observed. After a third bifurcation,  $R_\pi$  symmetry is lost and the flow becomes chaotic and turbulent. The spatial structure of the 3-D flow can be significantly different from that observed in axisymmetric simulations but the typical magnitude of the flow in both settings remains comparable.

One of the main objectives of this study was to provide deeper insights in the various scaling regimes that can exist in swirling EVFs. Simulations done over a wide range of parameters  $J$ ,  $B$  and  $\nu$  have allowed us to identify four flow regimes in which the flow intensity  $U$  is given by the following scaling laws:

$$U \sim \begin{cases} \frac{JBR^2}{\rho\nu} & \text{(inductionless, viscous regime),} \\ \left(\frac{JB}{\rho}\right)^{2/3} \frac{R}{\nu^{1/3}} & \text{(inductionless, laminar boundary layer regime),} \\ \left(\frac{JBR}{\rho}\right)^{1/2} \text{ or } \left(\frac{JBR}{\rho}\right)^{5/9} \left(\frac{R}{\nu}\right)^{1/9} & \text{(inductionless, inertial regime),} \\ \frac{J}{\sigma B} & \text{(inductive regime).} \end{cases} \quad (5.1)$$

The inductive scaling regime for high imposed magnetic fields was already investigated (Malcolm 1970; Hunt & Malcolm 1968). We find that this regime is not controlled by Hartmann or Shercliff layers. In the inductionless limit ( $\sigma UB/J \ll 1$ ), the viscous and inertial regimes are fairly classical and previously observed in Bojarevičs *et al.* (1989); Davidson *et al.* (1999); Kolesnichenko *et al.* (2020). The intermediate 2/3 scaling law reported by Herreman *et al.* (2021) is not really observable with the von Kármán-like EVFs. We think that the increased level of turbulence in the bulk of this flow likely has a drastic effect on the delicate three-term balance that governs this regime. The 2/3 law indeed requires a laminar boundary layer; see Appendix A and Davidson (1992). We also know that it exists as an intermediate regime in duct flows (Poyé *et al.* 2020; Vernet *et al.* 2021).

The geometry of the fluid domain and the radius of the wires have a strong impact on the EVF. We have proposed a simple model that suggests a parabolic decay of flow intensity with increasing wire radius  $R_w/R$ . In cells with small aspect ratios  $H/R$ , the flow is mostly intense above the electrical contact. Our simulations of asymmetrical current injection/withdrawal suggest that the 2/3 scaling law is more easily observed in this case and this is likely due to the fact that the unstable mixing layer is absent.

For future work, it would be interesting to study more precisely the transition between the laminar boundary layer regime (2/3) and the inertial regime (1/2). In particular, what happens in the boundary layer? To answer this question, we need extremely well-resolved 3-D simulations without any kind of turbulence model. It is not impossible that the use of turbulence models,  $k-\epsilon$  in Davidson *et al.* (1999),  $k-\omega$  in Kolesnichenko *et al.* (2020), prevent the subtle (2/3) laminar boundary layer scaling law from being observable. It would also be interesting to have direct numerical simulations of EVFs in other types of cells, such as a hemispherical device (Kharicha *et al.* 2015) or in a cylinder with a free surface (Kolesnichenko *et al.* 2020).

**Supplementary movie.** Supplementary movie is available at <https://doi.org/10.1017/jfm.2022.779>.

**Funding.** The HPC resources were provided by GENCI-IDRIS (grant 2021-0254) in France. J.-L. Guermond acknowledges support from University Paris-Saclay, the National Science Foundation, under grants NSF DMS 1620058, DMS 1619892, the Air Force Office of Scientific Research, USAF, under grant/contract number FA9550-18-1-0397, and the Army Research Office under grant/contract number W911NF-15-1-0517.

**Declaration of interests.** The authors report no conflict of interest.

**Author ORCIDs.**

✉ S. Bénard <https://orcid.org/0000-0002-6199-2598>;

✉ W. Herreman <https://orcid.org/0000-0002-3116-0280>;

✉ C. Nore <https://orcid.org/0000-0001-9118-5247>.

**Appendix A. The 2/3 scaling law in Davidson (1992), Davidson *et al.* (1999)**

The two- or three-term balance equations we have used in § 3.6 have the advantage of being conceptually simple, but they also hide that complex exchanges of momentum and energy occur between the boundary layer and the bulk regions. A finer approach has been proposed in Davidson (1992), where the author uses a method based on the balance of angular momentum to derive scaling laws in axisymmetric flows driven by azimuthal body forces per unit mass  $F_\theta$  in the stationary case. An example of such a global balance is

$$\rho \int_V r F_\theta \, dV + \int_{\delta V} r \tau_\theta \, dS = 0. \tag{A1}$$

The volume integral on the left-hand side is the torque induced by the volumic force, and the surface integral is the viscous torque. The term  $\tau_\theta$  is the viscous stress at the boundary. A particular situation considered in Davidson (1992) consists of assuming that the force  $F_\theta$  is due to a transverse magnetic field slowly rotating (magnetic stirring). Denoting by  $\omega$  the angular velocity of the magnetic field and assuming that  $\omega$  is not too large, this force is therein estimated on average to be close to

$$F_\theta = \Omega_f^2 r \quad \text{with} \quad \Omega_f = B \left( \frac{\sigma \omega}{\rho} \right)^{1/2}. \tag{A2}$$

Using laminar or turbulent wall friction laws for the viscous stress  $\tau_\theta$ , the following expressions for the intensity of the swirling bulk flow are derived in Davidson (1992, equations (25) and (26)):

$$U \sim \Omega_f R \left( \frac{\Omega_f R^2}{\nu} \right)^{1/3} \quad (\text{laminar}), \quad U \sim \Omega_f R \left( \frac{\Omega_f R^2}{\nu} \right)^{1/9} \quad (\text{turbulent}). \tag{A3}$$

At the end of § 3.1 in Davidson *et al.* (1999), the authors refer to these expressions when they briefly formulate turbulent scaling laws for swirling EVFs (see also (1.2) and the



related discussion in the introduction). Since the analogies made therein are not entirely clear to us, we propose to revisit this presentation and give a slightly different point of view. Using (A2), the above two scaling laws can be rewritten as  $U \sim F_\theta^{2/3} R/\nu^{1/3}$  in the laminar case and  $U \sim (F_\theta R)^{5/9} (R/\nu)^{1/9}$  in the turbulent case. Replacing the body force  $F_\theta \sim JB/\rho$  to cover the case of a swirling EVF, we obtain the following scaling laws for the flow intensity of the swirling EVF:

$$U \sim \left(\frac{JB}{\rho}\right)^{2/3} \frac{R}{\nu^{1/3}} \quad (\text{laminar}), \tag{A4a}$$

$$U \sim \left(\frac{JBR}{\rho}\right)^{5/9} \left(\frac{R}{\nu}\right)^{1/9} \quad (\text{turbulent}). \tag{A4b}$$

This simple argument yields the 5/9 scaling law of Davidson *et al.* (1999); it also recovers the 2/3 law that we have observed in our simulations and in Herreman *et al.* (2021). The 2/3 exponent is just the manifestation of a laminar boundary layer, with its laminar boundary layer friction law. The model of Davidson (1992), Davidson *et al.* (1999) also allows the 2/3 scaling law.

### Appendix B. Dependence of $U$ with respect to $R_w/R$

The method we propose to model the dependence of flow intensity on  $R_w/R$  is motivated by the torque balance of Davidson *et al.* (1999). Approximating the Lorentz force as  $\mathbf{j} \times \mathbf{B} \approx -j_r B \mathbf{e}_\theta$ , the axial torque balance between the Lorentz force and the viscous stress gives

$$\underbrace{\int_V r j_r B \, dV}_K \approx \int_{\delta V} r \tau_\theta \, dS. \tag{B1}$$

When  $V$  is the entire fluid domain, the left integral is zero due to symmetry. Let us consider this balance with  $V$ , the bottom half of the cell (similar to the asymmetrical cell with a thin wire connected at the bottom of the cell and an extended wire at the top). Considering that  $j_r \approx -\mu_0^{-1} \partial_z b_\theta$ , due to Ampère’s law, and supposing axisymmetry, the expression for the torque induced by the Lorentz force simplifies as

$$K = \frac{2\pi B}{\mu_0} \int_0^R (b_\theta|_{z=-H} - b_\theta|_{z=0}) r^2 \, dr. \tag{B2}$$

Since in our simulations we have access to the magnetic field at the top and bottom of the cell, the radial integral can be numerically evaluated. A theoretical approximation can also be obtained as follows. Since we enforce  $\mathbf{j}|_{z=0} = J \mathbf{e}_z$  at the top of the cell, we have

$$b_\theta|_{z=0} = \frac{\mu_0 I r}{2\pi R^2}. \tag{B3}$$

On the insulating part of the bottom surface, that is, for  $r \in [R_w, R]$ , the magnetic field is directly available from the boundary conditions (2.4) or Ampère’s law. Then recalling that  $I = J/\pi R^2$ , we obtain

$$\text{for } r \in [R_w, R], \quad b_\theta|_{z=-H} = \frac{\mu_0 I}{2\pi r}. \tag{B4a}$$

Above the electrical contact, for  $r \in [0, R_w]$ , we consider two limiting cases. It is shown in Herreman *et al.* (2019) that the Millere approximation is well adapted if the connecting

wire is very thin with respect to  $R$  (see Millere *et al.* 1980). If, instead, the connecting wire is thick, it is reasonable to assume that the current density is close to being uniform. These two limiting cases give

$$\text{for } r \in [0, R_w], \quad b_\theta|_{z=-H} = \frac{\mu_0 I}{2\pi} \begin{cases} (1 - \sqrt{1 - (r/R_w)^2})/r & \text{(Millere),} \\ r/R_w^2 & \text{(uniform).} \end{cases} \quad (\text{B4b})$$

With the above expressions, we then calculate the dependence of the torque (4.1) on  $R_w/R$  that is copied into that of the flow intensity (4.2).

#### REFERENCES

- ASHOUR, R.F., KELLEY, D.H., SALAS, A., STARACE, M., WEBER, N. & WEIER, T. 2018 Competing forces in liquid metal electrodes and batteries. *J. Power Sourc.* **378**, 301–310.
- BERHANU, M., *et al.* 2007 Magnetic field reversals in an experimental turbulent dynamo. *Europhys. Lett.* **77** (5), 59001.
- BOJAREVIČS, V., FREIBERGS, J.A., SHILOVA, E.I. & SHCHERBININ, E.V. 1989 *Electrically Induced Vortical Flows*. Mechanics of Fluids and Transport Processes, vol. 1. Springer.
- BOJAREVICIS, V., MILLERE, R. & CHAIKOVSKY, A.I. 1981 Investigation of the azimuthal perturbation growth in the flow due to an electric current point source. In *Proceedings of the 10th Riga Conference on MHD, Riga, Latvia*, vol. 1, pp. 147–148.
- CAPPANERA, L., GUERMOND, J.-L., HERREMAN, W. & NORE, C. 2018 Momentum-based approximation of incompressible multiphase fluid flows. *Intl J. Numer. Meth. Fluids* **86** (8), 541–563.
- CHUDNOVSKII, A.Y. 1989 Evaluating the intensity of a single class of electrovortex flows MHD. *Magnetohydrodynamics* **25** (3), 406–408.
- DAVIDSON, P.A. 1992 Swirling flow in an axisymmetric cavity of arbitrary profile, driven by a rotating magnetic field. *J. Fluid Mech.* **245**, 669–699.
- DAVIDSON, P.A. 2001 *An Introduction to Magnetohydrodynamics*. Cambridge Texts in Applied Mathematics. Cambridge University Press.
- DAVIDSON, P.A., KINNEAR, D., LINGWOOD, R.J., SHORT, D.J. & HE, X. 1999 The role of Ekman pumping and the dominance of swirl in confined flows driven by Lorentz forces. *Eur. J. Mech. (B/Fluids)* **18**, 693–711.
- GEINDREAU, C. & AURIAULT, J.-L. 2002 Magnetohydrodynamic flows in porous media. *J. Fluid Mech.* **466**, 343–363.
- GUERMOND, J.-L., LAGUERRE, R., LÉORAT, J. & NORE, C. 2007 An interior penalty Galerkin method for the MHD equations in heterogeneous domains. *J. Comput. Phys.* **221** (1), 349–369.
- GUERMOND, J.-L., LAGUERRE, R., LÉORAT, J. & NORE, C. 2009 Nonlinear magnetohydrodynamics in axisymmetric heterogeneous domains using a Fourier/finite element technique and an interior penalty method. *J. Comput. Phys.* **228**, 2739–2757.
- HERREMAN, W., BÉNARD, S., NORE, C., PERSONNETTAZ, P., CAPPANERA, L. & GUERMOND, J.-L. 2020 Solutal buoyancy and electrovortex flow in liquid metal batteries. *Phys. Rev. Fluids* **5**, 074501.
- HERREMAN, W., NORE, C., CAPPANERA, L. & GUERMOND, J.-L. 2021 Efficient mixing by swirling electrovortex flows in liquid metal batteries. *J. Fluid Mech.* **915**, A17.
- HERREMAN, W., NORE, C., ZIEBELL RAMOS, P., CAPPANERA, L., GUERMOND, J.-L. & WEBER, N. 2019 Numerical simulation of electrovortex flows in cylindrical fluid layers and liquid metal batteries. *Phys. Rev. Fluids* **4**, 113702.
- HUNT, J.C.R. & MALCOLM, D.G. 1968 Some electrically driven flows in magnetohydrodynamics. Part 2. Theory and experiment. *J. Fluid Mech.* **33** (4), 775–801.
- HUNT, J.C.R. & STEWARTSON, K. 1965 Magnetohydrodynamic flow in rectangular ducts. II. *J. Fluid Mech.* **23** (3), 563–581.
- KELLEY, D.H. & SADOWAY, D.R. 2014 Mixing in a liquid metal electrode. *Phys. Fluids* **26** (5), 057102.
- KELLEY, D.H. & WEIER, T. 2018 Fluid mechanics of liquid metal batteries. *Appl. Mech. Rev.* **70**, 020801.
- KHARICHA, A., TEPLYAKOV, I., IVOCHKIN, Y., WU, M., LUDWIG, A. & GUSEVA, A. 2015 Experimental and numerical analysis of free surface deformation in an electrically driven flow. *Exp. Therm. Fluid Sci.* **62**, 192–201.
- KOLESNICHENKO, I., FRICK, P., ELTISHCHEV, V., MANDRYKIN, S. & STEFANI, F. 2020 Evolution of a strong electrovortex flow in a cylindrical cell. *Phys. Rev. Fluids* **5** (12), 123703.

## *Simulations of swirling electrovortex flows in cylinders*

- LIU, K., STEFANI, F., WEBER, N., WEIER, T. & LI, B.W. 2020 Numerical and experimental investigation of electro-vortex flow in a cylindrical container. *Magnetohydrodynamics* **56** (1), 27–42.
- MALCOLM, D.G. 1970 An investigation of the stability of a magnetohydrodynamic shear layer. *J. Fluid Mech.* **41** (3), 531–544.
- MILLERE, R.P., SHARAMKIN, V.I. & SHCHERBININ, É.V. 1980 Effect of a longitudinal magnetic field on electrically driven rotational flow in a cylindrical vessel. *Magnetohydrodynamics* **1**, 81–85.
- MONCHAUX, R., *et al.* 2007 Generation of a magnetic field by dynamo action in a turbulent flow of liquid sodium. *Phys. Rev. Lett.* **98** (4), 044502.
- MORESCO, P. & ALBOUSSIÈRE, T. 2004 Experimental study of the instability of the Hartmann layer. *J. Fluid Mech.* **504**, 167–181.
- NORE, C., TARTAR, M., DAUBE, O. & TUCKERMAN, L.S. 2004 Survey of instability thresholds of flow between exactly counter-rotating disks. *J. Fluid Mech.* **511**, 45–65.
- NORE, C., TUCKERMAN, L.S., DAUBE, O. & XIN, S. 2003 The 1:2 mode interaction in exactly counter-rotating von Kármán swirling flow. *J. Fluid Mech.* **477**, 51–88.
- PLEVACHUK, Y., SKLYARCHUK, V., ECKERT, S., GERBETH, G. & NOVAKOVIC, R. 2014 Thermophysical properties of the liquid Ga–In–Sn eutectic alloy. *J. Chem. Engng Data* **59** (3), 757–763.
- POYÉ, A., AGULLO, O., PLIHON, N., BOS, W.J.T., DESANGLES, V. & BOUSSELIN, G. 2020 Scaling laws in axisymmetric magnetohydrodynamic duct flows. *Phys. Rev. Fluids* **5**, 043701.
- SUTTON, G.W. & SHERMAN, A. 1965 *Engineering Magnetohydrodynamics*. McGraw-Hill Book Company.
- VERNET, M., PEREIRA, M., FAUVE, S. & GISSINGER, C. 2021 Turbulence in electromagnetically driven Keplerian flows. *J. Fluid Mech.* **924**, A29.
- VLASYUK, V.K. 1987 Effects of fusible-electrode radius on the electrovortex flow in a cylindrical vessel. *Magnetohydrodynamics* **4**, 101–106.
- WEBER, N., GALINDO, V., PRIEDE, J., STEFANI, F. & WEIER, T. 2015 The influence of current collectors on Tayler instability and electro-vortex flows in liquid metal batteries. *Phys. Fluids* **27** (1), 014103.
- WEBER, N., NIMTZ, M., PERSONNETAZ, P., SALAS, A. & WEIER, T. 2018 Electromagnetically driven convection suitable for mass transfer enhancement in liquid metal batteries. *Appl. Therm. Engng* **143**, 293–301.
- WEBER, W., NIMTZ, M., PERSONNETAZ, P., WEIER, T. & SADOWAY, D. 2020 Numerical simulation of mass transfer enhancement in liquid metal batteries by means of electro-vortex flow. *J. Power Sources Adv.* **1**, 100004.